



저작자표시-비영리-변경금지 2.0 대한민국

이용자는 아래의 조건을 따르는 경우에 한하여 자유롭게

- 이 저작물을 복제, 배포, 전송, 전시, 공연 및 방송할 수 있습니다.

다음과 같은 조건을 따라야 합니다:



저작자표시. 귀하는 원저작자를 표시하여야 합니다.



비영리. 귀하는 이 저작물을 영리 목적으로 이용할 수 없습니다.



변경금지. 귀하는 이 저작물을 개작, 변형 또는 가공할 수 없습니다.

- 귀하는, 이 저작물의 재이용이나 배포의 경우, 이 저작물에 적용된 이용허락조건을 명확하게 나타내어야 합니다.
- 저작권자로부터 별도의 허가를 받으면 이러한 조건들은 적용되지 않습니다.

저작권법에 따른 이용자의 권리는 위의 내용에 의하여 영향을 받지 않습니다.

이것은 [이용허락규약\(Legal Code\)](#)을 이해하기 쉽게 요약한 것입니다.

[Disclaimer](#)

Master's Thesis

Electrolyte containing 1-ethoxy-2-methoxy ethane  
and lithium difluoro(bisoxalato) phosphate to  
improve fast charging capability of high-energy Li-  
ion batteries

Somi Lee

Department of Energy Engineering  
(Battery Science and Technology)

Graduate School of UNIST

2020

Electrolyte containing 1-ethoxy-2-methoxy ethane  
and lithium difluoro(bisoxalato) phosphate to  
improve fast charging capability of high-energy  
Li-ion batteries

Somi Lee

Department of Energy Engineering  
(Battery Science and Technology)

Graduate School of UNIST

Electrolyte containing 1-ethoxy-2-methoxy ethane  
and lithium difluoro(bisoxalato) phosphate to  
improve fast charging capability of high-energy Li-  
ion batteries

A thesis/dissertation  
submitted to the Graduate School of UNIST  
in partial fulfillment of the  
requirements for the degree of  
Master of Science

Somi Lee

06/12/2020

Approved by



Advisor

Nam-Soon Choi

Electrolyte containing 1-ethoxy-2-methoxy ethane  
and lithium difluoro(bisoxalato) phosphate to  
improve fast charging capability of high-energy  
Li-ion batteries

Somi Lee

This certifies that the thesis/dissertation of Somi Lee is approved.

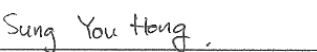
06/12/2020

signature




Advisor: Nam-Soon Choi

signature



Sung You Hong

signature



Seok Ju Kang

## Abstracts

With the advent of the era of electric vehicles, the demand for high energy density lithium ion batteries with fast charging capability is increasing. In order to increase the energy density of lithium ion batteries, high loading level of the electrode is required. However, the electrode with high loading level has the disadvantage that impregnation of electrolyte decreases and lithium ion diffusion is not facile due to the long Li ion pathway. In this regard, research on low-viscosity solvents that improve electrolyte impregnation and have high ionic conductivity is inevitable. Conventional low-viscosity solvents have high volatility, causing gas generation. Gas generation results in pouch swelling issues, deteriorating safety of the batteries. In this paper, a low-viscosity 1-ethoxy-2-methoxy ethane (EME) solvent with high boiling point is used. In the TGA and pouch swelling test, EME shows lower volatility and less gas evolution. By introducing EME with high ionic conductivity, interfacial resistance reduces and fast charging performance improves. However, the unstable surface film formed by EME is not able to prevent dissolution of metal ions at high temperature, inducing capacity fading. To prevent these side reactions, Lithium difluoro (bisoxalato) phosphate (LiDFBP), which decomposes before EME, is introduced. It is confirmed through dQ/dV graph that the LiDFBP additive inhibites the decomposition of EME and forms a stable film on the surface of the electrodes. The stable CEI layer formed by decomposition of LiDFBP additives hinders dissolution of transition metal ions and microcrack generation of the NCM811 cathode. During cycling test, the SEI layer derived from LiDFBP additive suppresses the formation of Li dendrite and byproducts on the surface of the anode. This study, which introduces a low-viscosity EME solvent and overcomes disadvantages of EME, suggests the direction in which low-viscosity solvent research should proceed.

## Contents

### 1. INTRODUCTION

1.1. Lithium-ion battery.....	1
1.2. For high capacity of LIBs.....	3
1.2.1. Introduction of Ni-rich cathode.....	3
1.2.2. Introduction of Silicon as anode.....	5
1.2.3. High-mass-loading electrode.....	7
1.3. Improvement strategies with electrolyte.....	9
1.3.1. Solvent with low viscosity.....	9
1.3.2. SEI and CEI forming additives.....	11
1.3.3. Functional electrolyte design for fast charging capability.....	14

### 2. EXPERIMENTAL

2.1. Preparation of electrolytes and electrodes.....	15
2.2. Electrochemical measurements.....	16
2.3. Characterization.....	17

### 3. RESULTS AND DISCUSSION

3.1. Effect of low viscous EME solvent.....	19
3.2. Introduction of LiDFBP additive to complement EME solvent.....	28

### 4. CONCLUSION.....

### 5. REFERENCES.....

## List of figures

**Figure 1.** Requirements of future LIBs.

**Figure 2.** Schematic diagram of LIB.

**Figure 3.** Theoretical capacity of cathode materials and layered transition metal oxides.

**Figure 4.** Schematic diagram of possible cation mixing path in the charged NMC811 cathode.

**Figure 5.** Microcrack generation scheme of NCM cathodes.

**Figure 6.** Candidates of active anode materials for the post lithium batteries.

**Figure 7.** The regarding problems with using Si as anode.

**Figure 8.** (a) Average discharge voltages depending on cathode thickness under various rates. (b) Volumetric energy density depending on cathode thickness under various rates.

**Figure 9.** (a) SEM image of cycled graphite anodes retrieved from NCM/graphite full cells. (b) Cross-sectional SEM image of cycled graphite anodes retrieved from NCM/graphite full cells. Yellow arrows indicate Li dendrites. Red dotted lines indicate thick SEI layer caused by electrolyte decomposition on the surface of the graphite anode.

**Figure 10.** Rate capacity and cycle retention of the half-cells using different carbonate solvents.

**Figure 11.** (a) Reduction mechanism of VC. (b) Reduction mechanism of FEC.

**Figure 12.** Cycle test of Si@C with different electrode masses ( $m_E$ ). The cells were cycled in the voltage range of 0.01-1.2V at a current density of 0.25 mA/cm<sup>2</sup>, 0.5 mA/cm<sup>2</sup> and 1 mA/cm<sup>2</sup> with FEC or VC.

**Figure 13.** Schematic diagram showing the effect of FEC and VC on silicon anode.

**Figure 14.** Schematic diagram showing the effect of LiDFBP on Li-rich cathode.

**Figure 15.** Schematic illustration of concentration gradient of Li ion in electrolyte when starting charge with high current density.

**Figure 16.** TGA of electrolytes containing solvents and lithium salts only without additives.

**Figure 17.** (a) Changes in the thickness of the pouch-type full cells stored at 45°C. (b) Changes in the thickness of the pouch-type full cells stored at 60°C.

**Figure 18.** (a) Viscosity (points and left side y axis) and Conductivity (bars and right side y axis) values of Carbonate and EME. (b) Photographs of electrolyte's contact angle on NCM811 cathode.

**Figure 19.** (a) The impedances spectra of NCM811/gra-SiC full cells with Carbonate and EME after precycles. (b) Comparison of the charge rate capability of NCM811/gra-SiC full cells with Carbonate and EME.



**Figure 20.** XRD patterns of charged NCM811 cathode at 4C-rate after precycles.

**Figure 21.** Floating test of NCM811/Li half cells charged 4.3V at 25°C.

**Figure 22.** LSV of Carbonate and EME at 60°C.

**Figure 23.** Transition metal dissolution degree analyzed by inductively coupled plasma (ICP). Charged cathodes with Carbonate were stored in (a) Carbonate electrolyte and (b) EME electrolyte. (c) Charged cathode with EME.

**Figure 24.** Hydrolysis reactions of  $\text{LiPF}_6$  salt in the presence of water in the cell.

**Figure 25.**  $^{19}\text{F}$  NMR spectra with (a) Carbonate (b) EME storing for 20 days at 45 °C.

**Figure 26.** Chemical structure of (a) 1-ethoxy-2-methoxy ethane (EME) and (b) Lithium difluoro(bisoxalato) phosphate (LiDFBP). (c) HOMO and LUMO energy level of EME, FEC, and LiDFBP.

**Figure 27.**  $dQ/dV$  plot of NCM811/gra-SiC full cells with Carbonate, Carbonate+LiDFBP, EME, and EME + LiDFBP during first lithiation.

**Figure 28.** LSV of EME and EME + LiDFBP at 60°C.

**Figure 29.** O 1s and F 1s XPS spectra of NCM811 cathodes from NCM811/gra-SiC full cells after formation cycle (EME : (a), (c); and EME + LiDFBP : (b), (d)).

**Figure 30.** Possible mechanisms for SEI formation by the oxidative decomposition of LiDFBP.

**Figure 31.** BSE images from the cross-sectional SEM of NCM811 cathodes (a), (c), (e) cycled with EME and (b), (d), (f) cycled with EME + LiDFBP. Red arrows indicate microcracks of the cathode.

**Figure 32.** Schematic illustration of effects of LiDFBP-derived CEI on deterioration of the NCM811 cathode.

**Figure 33.** (a) Schematic illustration of transition metal dissolution test. (b) Transition metal dissolution degree analyzed by inductively coupled plasma (ICP). (c) Schematic illustration of beneficial effects of LiDFBP additive on transition metal dissolution, migration, and deposition processes. (d) Ni 2p XPS spectra of NCM811 cathode extracted from NCM811/gra-SiC full cells after 50 cycles at 45°C. (e) Ni 2p spectra of gra-SiC anode extracted from NCM811/gra-SiC full cells after 50 cycles at 45°C.

**Figure 34.** (a) C 1s, (b) F 1s, and (c) O 1s XPS spectra of NCM811 cathodes from NCM811/gra-SiC full cells after precycle.

**Figure 35.** The top-view and the cross-sectional SEM images of gra-SiC anode obtained from the NCM811 /gra-SiC full cell with (a), (d) Carbonate , (b), (e) EME, and (c), (f) EME + LiDFBP after 50cycles at 45 °C.

**Figure 36.** C 1s, F 1s, and O 1s XPS spectra of NCM811 cathodes from NCM811/gra-SiC full cells after 50 cycles at 45°C (Carbonate : (a), (b), (c); EME : (d), (e), (f); and EME + LiDFBP : (g), (h), (i)).

**Figure 37.** Possible decomposition mechanisms of EME.

**Figure 38.** Schematic illustration of beneficial effects of LiDFBP on the anode.

## **List of tables**

**Table 1.** Physical properties of conventional solvents and 1-ethoxy-2-methoxy ethane (EME).

**Table 2.** Composition of electrolytes.

# 1. Introduction

## 1.1. Lithium-ion battery

With rapidly increasing demands for energy storage devices, rechargeable Lithium ion batteries (LIBs) are regarded as one of the most crucial energy conversion and storage device. LIBs have been used in a wide range of applications from portable electric devices to energy systems. Even though LIBs have been successfully commercialized, superior LIBs with low cost, high capacity, safety and high power are required to satisfy the needs of many applications such as power tools, electric vehicles (EVs) and energy storage system (ESS). In particular, popularization of EVs depends on the development of rechargeable LIBs with higher energy density and fast-charging capability (**Figure 1**). [1, 2]

LIBs are energy conversion and storage device. LIBs consist of the four main components, cathode, anode, separator and electrolyte. During the charging process, the lithium ions move from cathode to anode. [3] During the discharge process, lithium ions come out of the negative electrode and moves to the positive electrode. The separator is a porous polymer film that prevents short-circuit from directly contacting the anode and cathode. The electrolyte is composed of solvent and additive and becomes a channel through which lithium ions can move.

For leap to the superior battery (e.g. high-capacity, high-power), the features of each material and interaction between materials should be considered to be properly used in different systems. Further researches on the electrolyte itself, electrodes and electrolyte surfaces are also required for the corresponding demand characteristics to the LIBs as the batteries which expands high energy density market. [4]

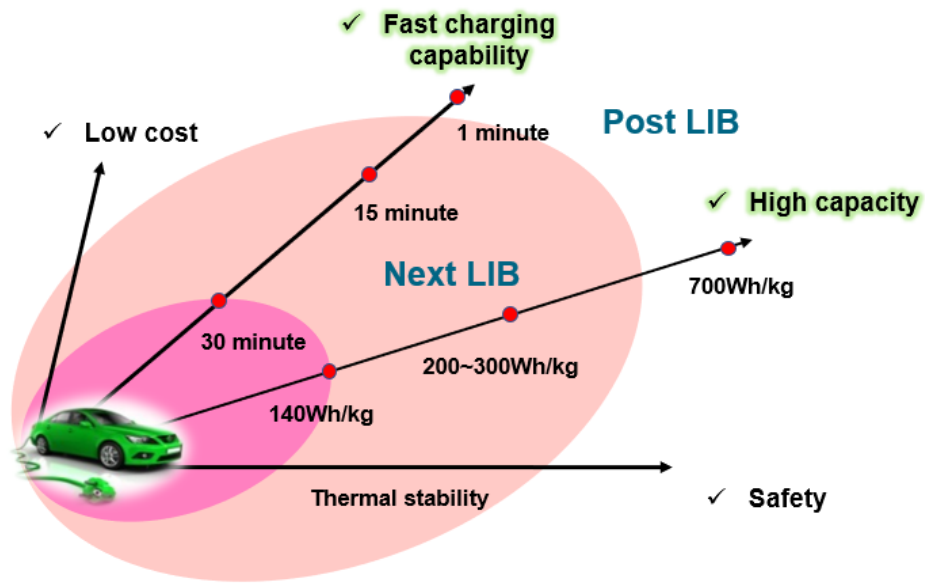


Figure 1. Requirements of future LIBs.

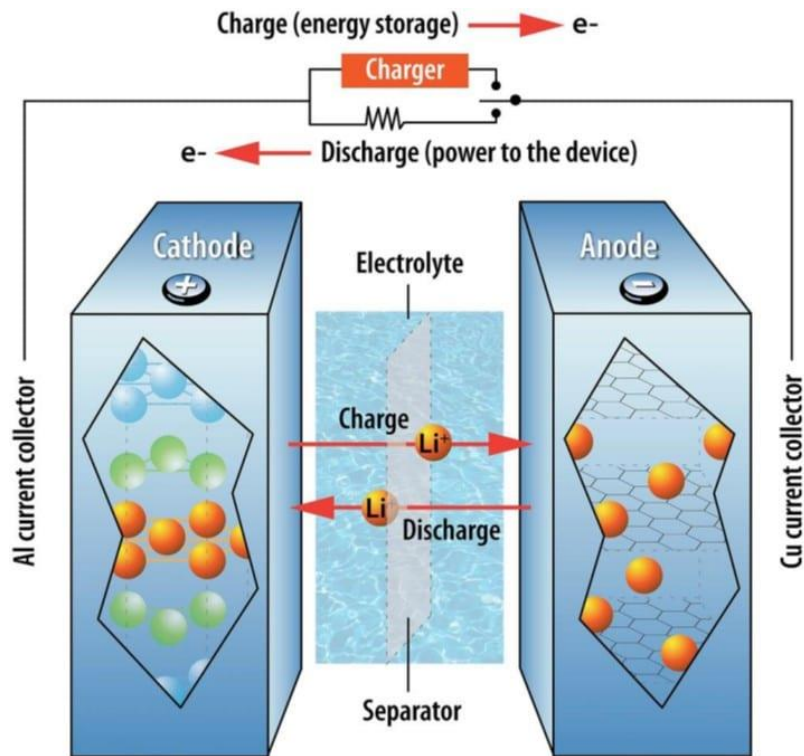


Figure 2. Schematic diagram of LIB.

1.2. For high capacity of LIBs

### 1.2.1. Introduction of Ni-rich NCM

Among the four main materials composing LIBs, a cathode containing the Li-ions decides the capacity of Lithium ion batteries. Recently, many researchers have focused on developing layered transition metal oxides as cathode materials. Among a variety of layered transition metal oxides, nickel-rich cathode materials such as  $\text{LiNi}_{0.8}\text{Co}_{0.1}\text{Mn}_{0.1}\text{O}_2$  (NCM811) and  $\text{LiNi}_{0.8}\text{Co}_{0.1}\text{Al}_{0.1}\text{O}_2$  (NCA811) are the most promising candidates with respect to high capacity and energy density (**Figure 3**). [5, 6] This is because nickel ions can be oxidized from 2+ to 4+, resulting in high reversible capacity. However, the cathodes with nickel content above 80% still have many issues in the commercialization in terms of stability and cost. [7] Structural instability of divalent nickel ions and tetravalent nickel ions causes phase transition by cation mixing (**Figure 4**). [8] The presence of nickel ions in the lithium layers interrupts the Li ion diffusion that is detrimental to fast charging capability. Moreover, phase transition caused by cation mixing leads to microcracks and transition metal dissolution (**Figure 5**). [9] Dissolved transition metal ions from the cathode can deposit on the surface of the anode, forming thick and resistive SEI layer.

For improving properties, many researchers try to diverse strategies such as doping, surface modification and so on.

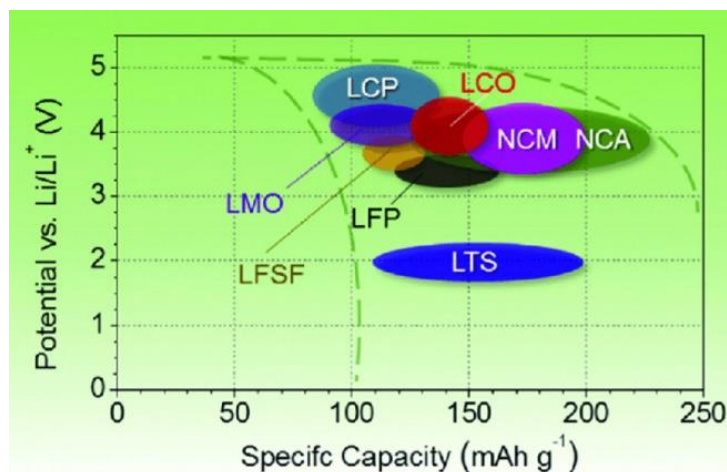


**Figure 3.** Theoretical capacity of cathode materials and layered transition metal oxides. [5]

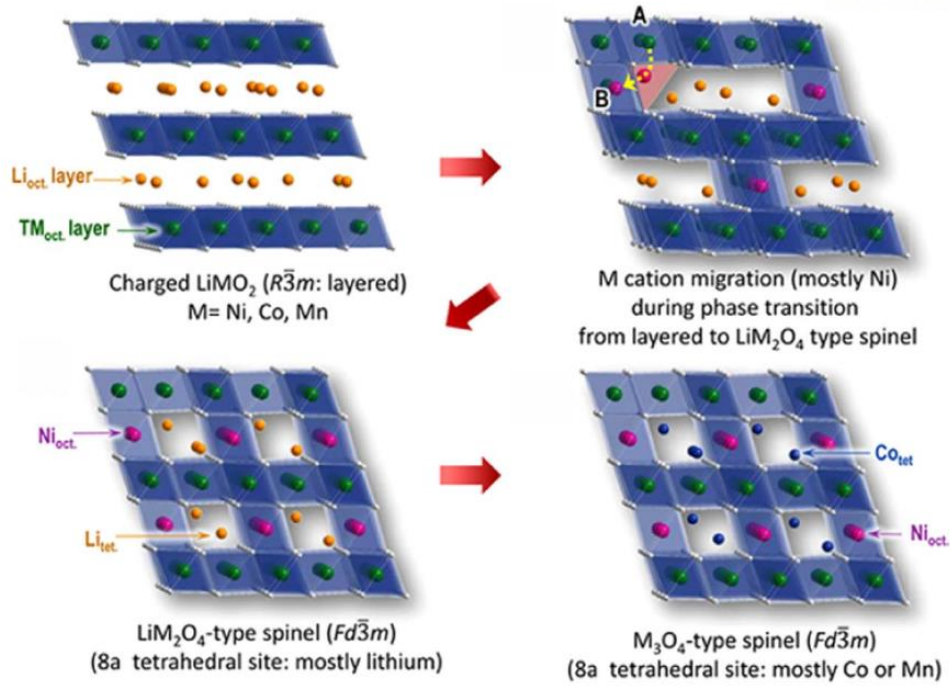


Figure 4. Schematic diagram of possible cation mixing path in the charged NMC811 cathode. [8]

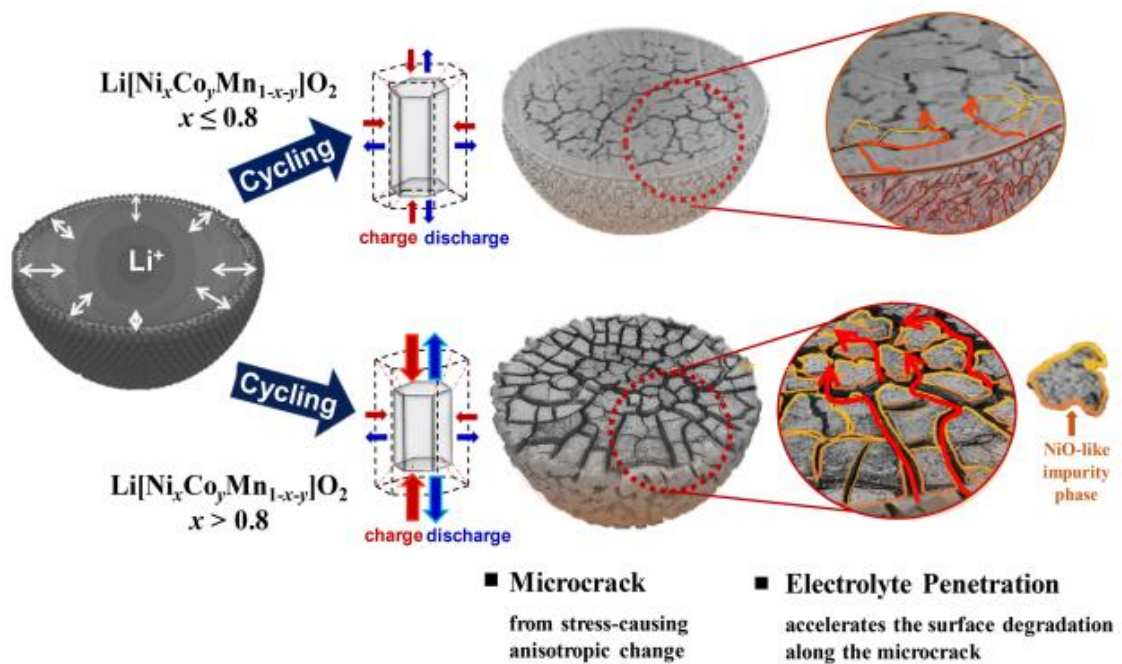


Figure 5. Microcrack generation scheme of NCM cathodes. [9]

### 1.2.2. Introduction of silicon as anode

The anode materials are also main materials for determining the capacity which can accommodate the Li-ions from the cathode. [10] For these requirements, graphite has become currently the most suitable material and is widely used as the anode for LIBs. However, to realize the greater capacity of the anode materials, there are many attempts to find the substances beyond the graphite (~372mAh/g) such as using Si, Sn, Ge and Sb atoms.

Si anode is one of the most practical anode materials in that the theoretical capacity is ten times higher than graphite (~4200 mAh/g for  $\text{Li}_{4.4}\text{Si}$  versus 372 mAh/g for  $\text{LiC}_6$ ). However, Si anode undergoes severe volumetric expansion by alloying reaction with Li-ions (**Figure 6**). In addition, Silicon has greater affinity between water and HF than graphite, forming an irreversible combination, which also causes loss of Si active material.

The anode material with the composition of Si and graphite can be one way to reduce the side reaction and get the advantages of high capacity. In this paper, the graphite-silicon coated graphite and graphite (gra-SiC) are introduced. [11] However, many issues of the Si still remained upon repeated cycling and leads to the pulverization of Si alloy and coated silicon, causing repeated damage to the surface (**Figure 7**). [12] Also, it can lead delamination from the current collector. These also can be solved with the additives forming solid electrolyte interphase (SEI). The stable SEI layer tolerating the volumetric strain of Si and preventing decomposition of electrolyte improves cycle life of LIBs.



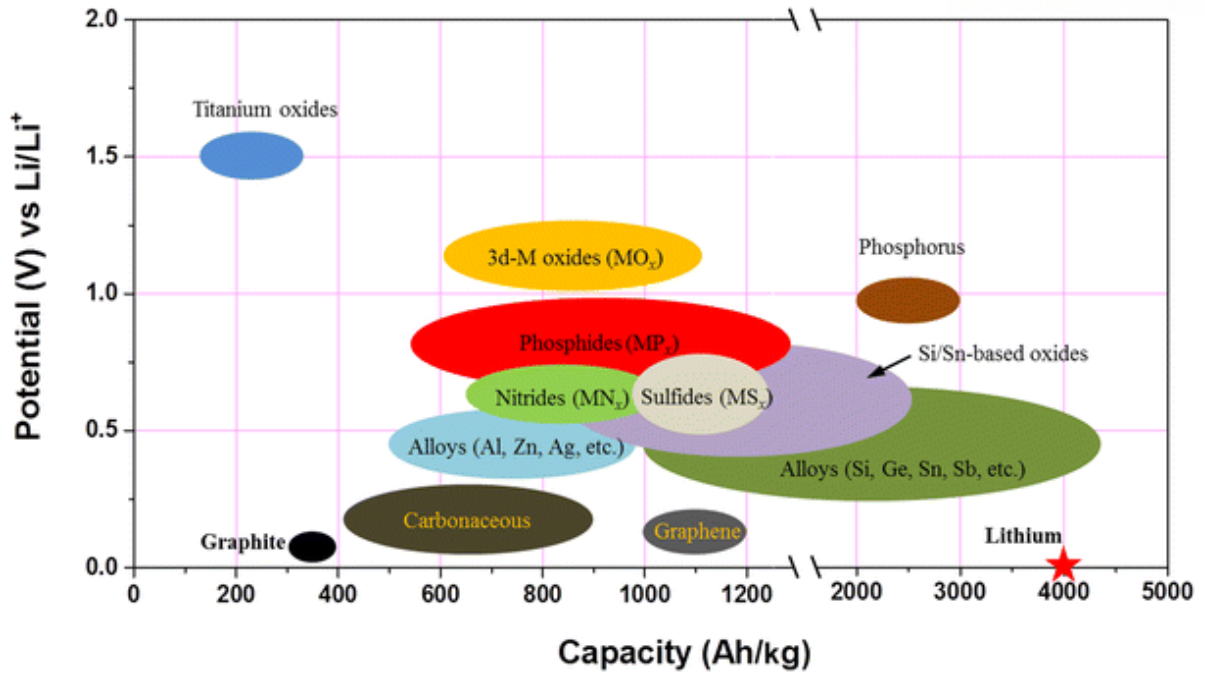


Figure 6. Candidates of active anode materials for the post lithium batteries. [10]

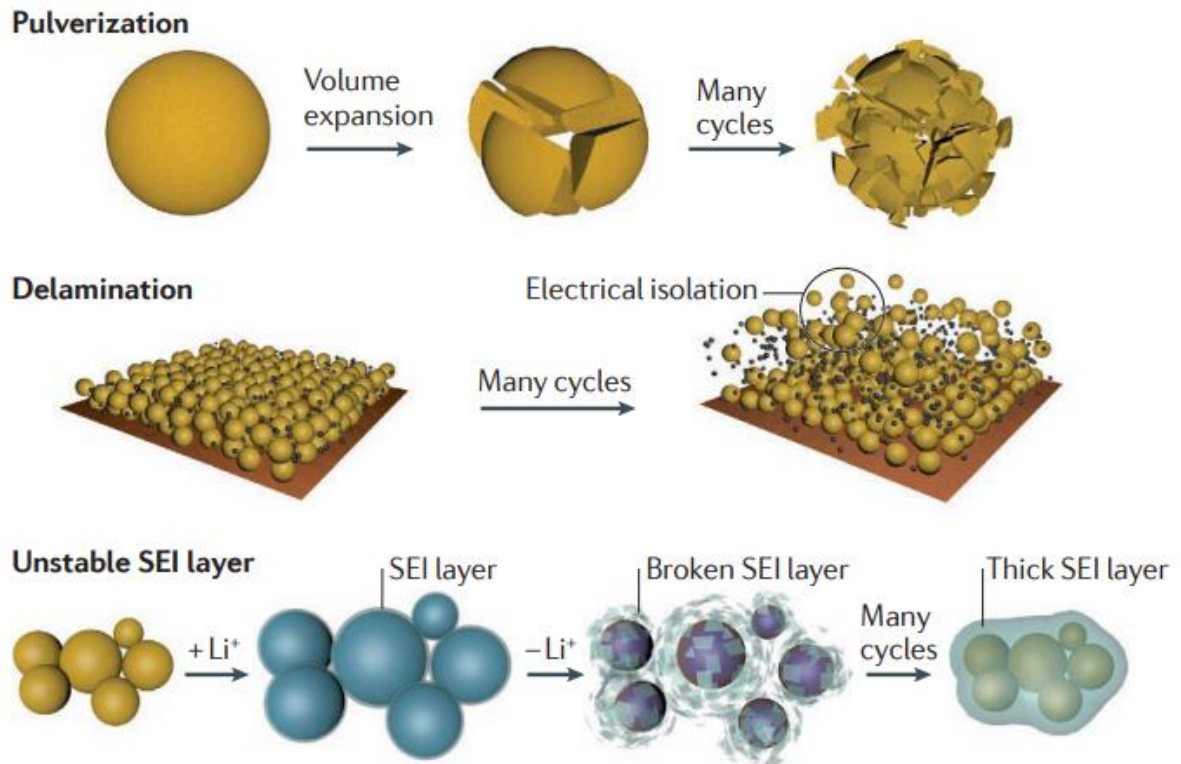


Figure 7. The regarding problems with using Si as anode. [12]

### 1.2.3. High-mass-loading electrode

The augmentation in thickness can multiply the amount of active materials, increasing energy density. However, since the thick electrode is not smoothly impregnated with an electrolyte, capacity fading occurs due to a decrease in the electrode utilization rate. In addition, as the pathway of Li ion becomes longer, the Li ion diffusion rate decreases and the fast charging performance deteriorates.

During fast charging, high concentration Li ions flow into the electrolyte from the electrode, increasing viscosity of the electrolyte around the active materials. The rapid increase in the viscosity of the electrolyte because of the high concentration lithium ions at the solid-electrolyte interface induces overpotential. When the applied current increased regularly to  $C/2$ ,  $1C$ , and  $2C$ , the polarization is increasingly pronounced in the thicker electrode, as shown in **Figure 8a**. The decrease in the cell voltage due to polarization results in the lower reversible capacity, offsetting the benefit from the thick electrode (**Figure 8b**). [13]

In addition, when high concentrations of lithium ions delithiated from the positive electrode during the rapid charging process is not smoothly lithiated into the structure of the negative electrode, lithium ions precipitate in the form of lithium metal on the surface of the negative electrode (**Figure 9a**). The metallic lithium directly causes an irreversible decomposition reaction of the electrolyte by directly contacting the surrounding electrolyte. If the side reaction of the electrolyte continues, a thick film is formed on the surface of the anode and the electrolyte introduced limitedly inside the battery is exhausted, thereby shortening the battery life (**Figure 9b**). [14]

To solve problems of high-mass loading electrode, the proper functions of electrolytes are required. The electrolyte becomes more important to maximize the impregnation of the electrolyte into the pores of the electrode and stabilize the interface.

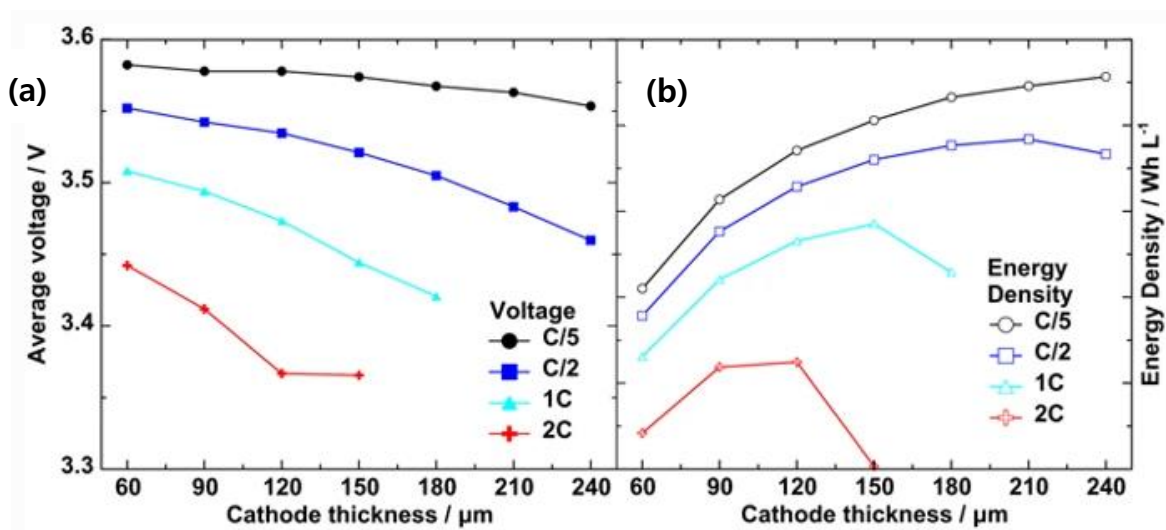


**Figure 8.** (a) Average discharge voltages depending on cathode thickness under various rates. (b) Volumetric energy density depending on cathode thickness under various rates. [13]

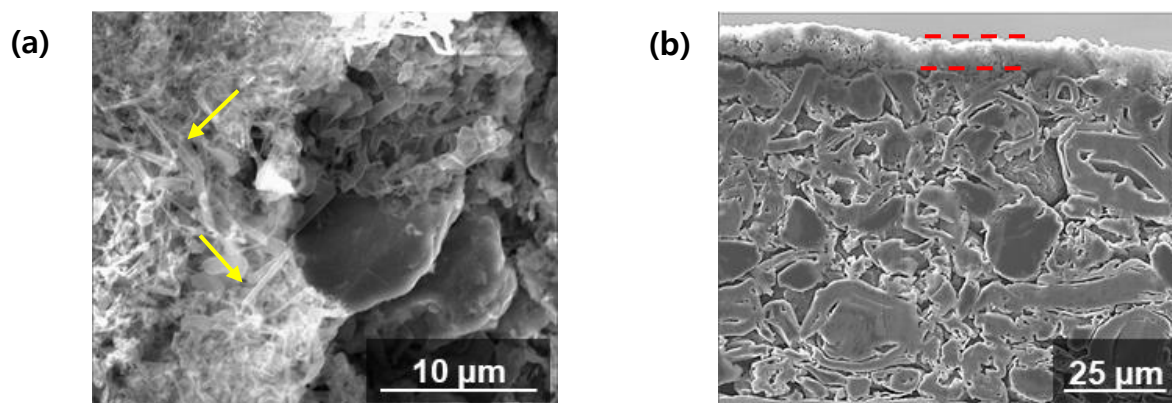


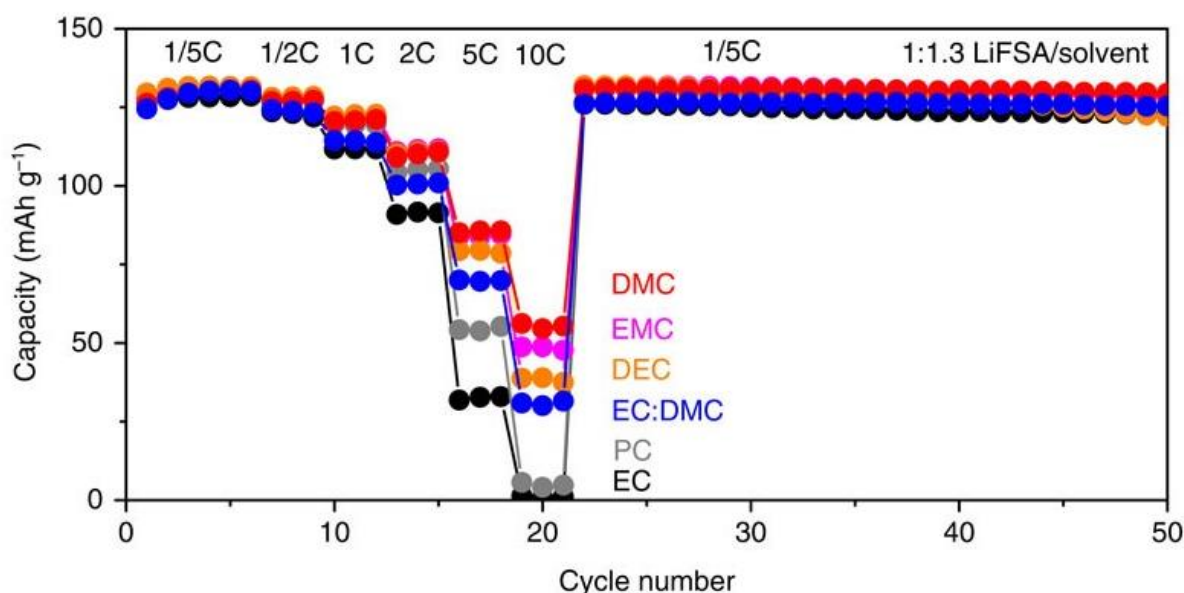
**Figure 9.** (a) SEM image of cycled graphite anodes retrieved from NCM/graphite full cells. (b) Cross-sectional SEM image of cycled graphite anodes retrieved from NCM/graphite full cells. Yellow arrows indicate Li dendrites. Red dotted lines indicate thick SEI layer caused by electrolyte decomposition on the surface of the graphite anode. [14]

### 1.3. Improvement strategies with electrolyte

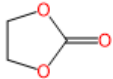
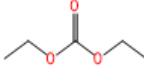
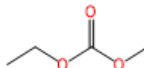
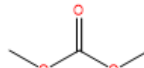
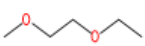
#### 1.3.1. Solvent with low viscosity

To improve fast charging capability of high-energy-density Lithium ion batteries, solvent is the most important factor. There are two crucial factors for choosing low-viscosity solvent to improve fast charging capability of the battery. [15] The first factor is how much low-viscosity solvent improves rate capabilities. [16] **Figure 10** shows that the lower the viscosity of the solvent, the better the rate capability. [17] This is because low-viscosity solvent enables facile Li ion diffusion. Dimethyl carbonate (DMC) is a representative low-viscosity solvent with a viscosity of 0.59 cP (**Table 1**).

Since most low-viscosity solvents generate gas due to low boiling point, high boiling point is also an important factor to enhance safety. DMC has a low boiling point of 90°C, which has a problem of generating gas at a high temperature. This gas evolution eventually leads to a pouch swelling issue, which is directly related to the safety of the battery. Therefore, it is necessary to introduce a low-viscosity solvent without causing a pouch swelling issue due to its high boiling point. [18] 1-ethoxy-2-methoxy ethane (EME) has a low viscosity of 0.52 cP and a high boiling point of 102 °C. In this paper, EME is utilized as a cosolvent. [19]



**Figure 10.** Rate capacity and cycle retention of the half-cells using different carbonate solvents. [17]

	Ethylene carbonate (EC)	Diethyl carbonate (DEC)	Ethyl methyl carbonate (EMC)	Dimethyl carbonate (DMC)	1-ethoxy-2-methoxy ethane (EME)
<b>Structure</b>					
<b>M.W. (g/mol)</b>	88.06	118.13	104.10	90.00	104.15
<b>m.p.(°C)</b>	36	-43	-14	3	-
<b>b.p.(°C)</b>	243	126.8	107	90	102
<b>Viscosity (cP, 25 °C)</b>	1.95 (@40°C)	0.75	0.65	0.59	0.52

**Table 1.** Physical properties of conventional solvents and 1-ethoxy-2-methoxy ethane (EME).

### 1.3.2. SEI and CEI forming additives

To improve fast charging capability of high-energy LIBs, the proper functions of additives are required. In particular, a single additive often cannot enable multifunctional properties. The use of mixed additives is imperative. [20]

The pulverization of silicon anode should be prevented to raise cycle life of the battery. One of the most effective strategies to overcome capacity fading is the use of additives. Proper additives have the ability to develop a stable SEI on anode material in LIB. Vinylene carbonate (VC) and fluoroethylene carbonate (FEC) additives are the best-known additives to protect anodes by reductive decomposition due to their low lowest unoccupied molecular orbital (LUMO). In case of VC, the presence of double bonds in VC structure leads to faster reduction than other carbonate solvents and forms polycarbonate components named in poly(VC) as shown in **Figure 11a**. VC is an efficacious additive to organize a stable SEI on graphite anodes, rising the capacity retention and thermal stability (**Figure 12**). On the other hand, FEC forms LiF-containing thin SEI which can accommodate the large volume changes of silicon during lithiation (**Figure 11b**). [21, 22, 23, 24] The FEC-derived SEI shows less reversibility compared to VC, but provides superior conductivity for Li ions, enhancing the rate capability of the anode. As a result, using a mixture of VC and FEC additives can boost cycle stability and rate capability of the Silicon-containing anodes (**Figure 13**). [23, 25]

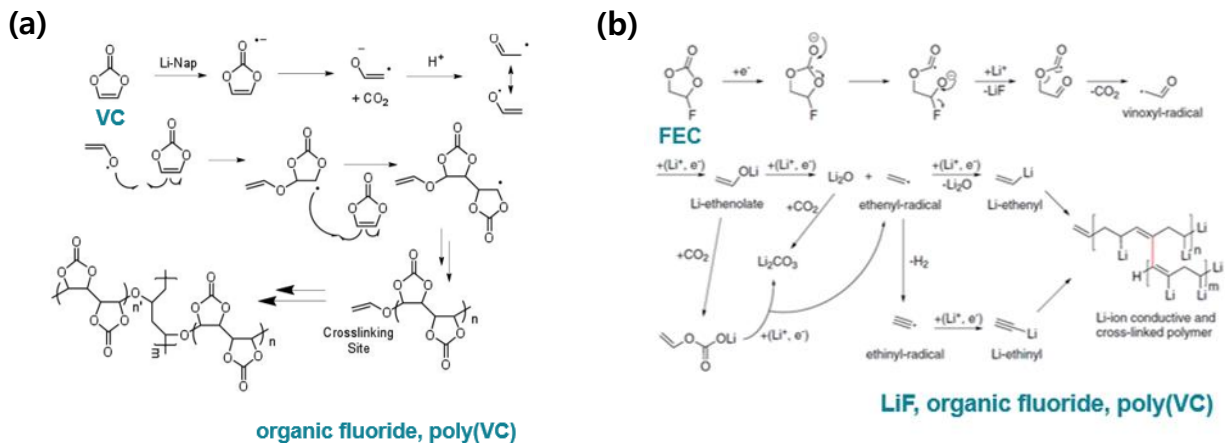


**Figure 11.** (a) Reduction mechanism of VC. (b) Reduction mechanism of FEC. [23]

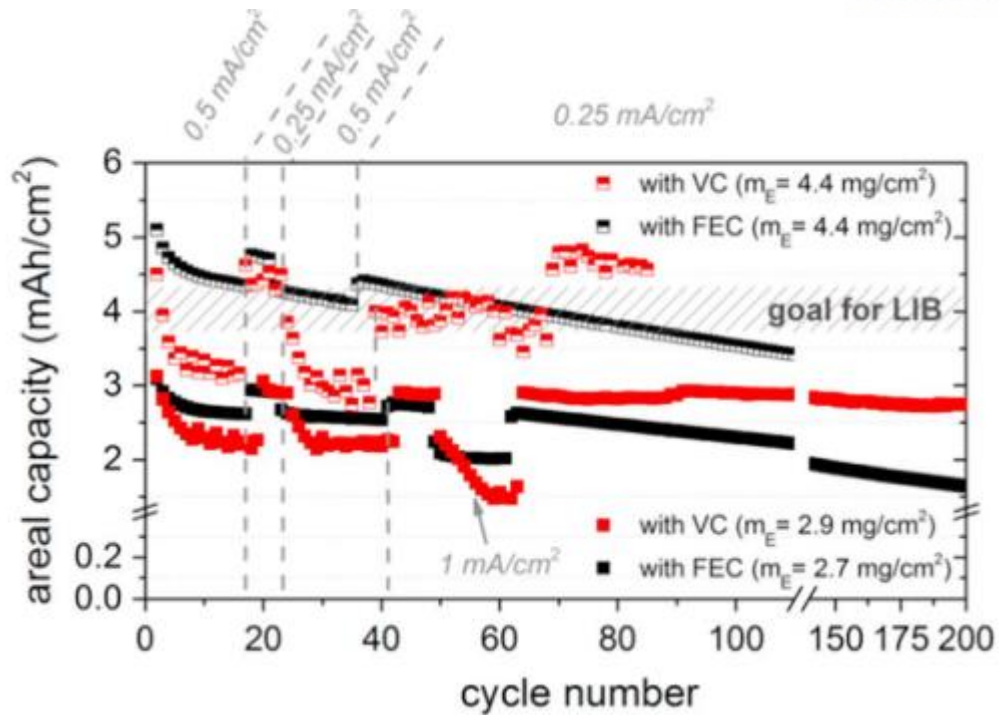


**Figure 12.** Cycle test of Si@C with different electrode masses ( $m_E$ ). The cells were cycled in the voltage range of 0.01-1.2V at a current density of 0.25 mA/cm<sup>2</sup>, 0.5 mA/cm<sup>2</sup> and 1 mA/cm<sup>2</sup> with FEC or VC. [25]

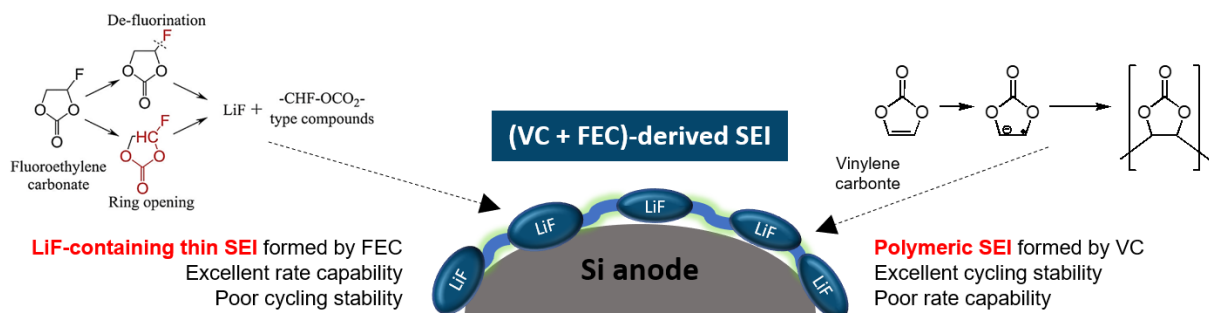


**Figure 13.** Schematic diagram showing the effect of FEC and VC on silicon anode.

In the case of cathode, the protective cathode electrolyte interphase (CEI) layer must be formed to prevent side reactions with residual lithium, highly oxidative  $\text{Ni}^{4+}$ , and electrolyte on the surface. Additionally, the well-made CEI layer can effectively prevent structural deformation of Ni-rich cathode during cycle and mitigate the further formation of microcracks. Lithium difluoro(bisoxalato) phosphate (LiDFBP) is one of the lithium salt type additives. LiDFBP additive forms P-O based uniform SEI on the anode and cathode due to its low lowest unoccupied molecular orbital (LUMO) and high highest occupied molecular orbital (HOMO). [26] Additives with high HOMO easily loses the electrons. Likewise, additives with low LUMO is favorable for reductive decomposition at the anode, easily getting the electrons. In addition, polar moieties (B-O, P-O, S=O) of additives form ionically conductive SEI, increasing rate capability of the battery. [27] To boost fast charging capability of the Li-ion batteries, formation of low resistive and ion-conducting SEI is critical. LiDFBP-derived CEI also prevents HF attack and alleviates phase transition of the cathode (**Figure 14**).

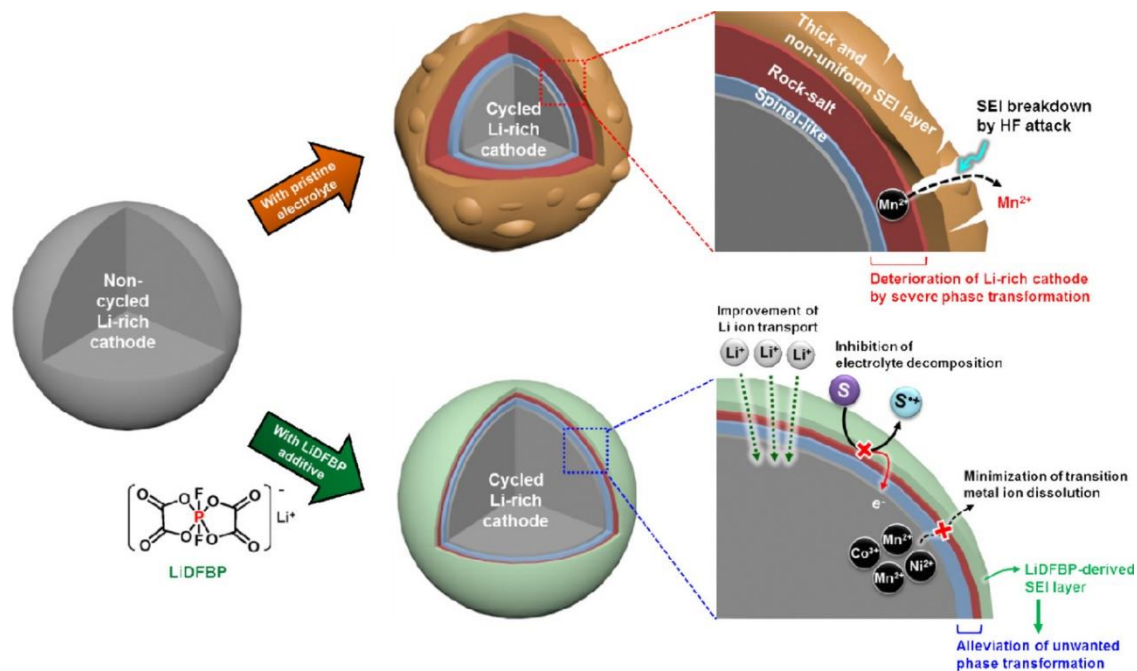


**Figure 14.** Schematic diagram showing the effect of LiDFBP on Li-rich cathode. [26]



### 1.3.3. Functional electrolyte design for fast charging capability

To improve fast charging capability of high energy Lithium ion batteries, the proper functions of electrolytes are required for each step. As mentioned above statement, to improve Li ion diffusion and electrolyte impregnation, low viscous 1-ethoxy-2-methoxy ethane (EME) cosolvent is adopted. Unlike other conventional low-viscosity solvents, EME solvent which has high boiling point is less volatile and does not cause pouch swelling issue. On the other hand, VC and FEC are used to overcome problems of Silicon anode and improves cycling stability. LiDFBP is utilized to hamper decomposition of electrolyte and protect the electrode from HF attack at high temperature. LiDFBP additive also contributes to formation of less resistive and ionically conductive film, mitigating Li dendrite growth during fast charging process.

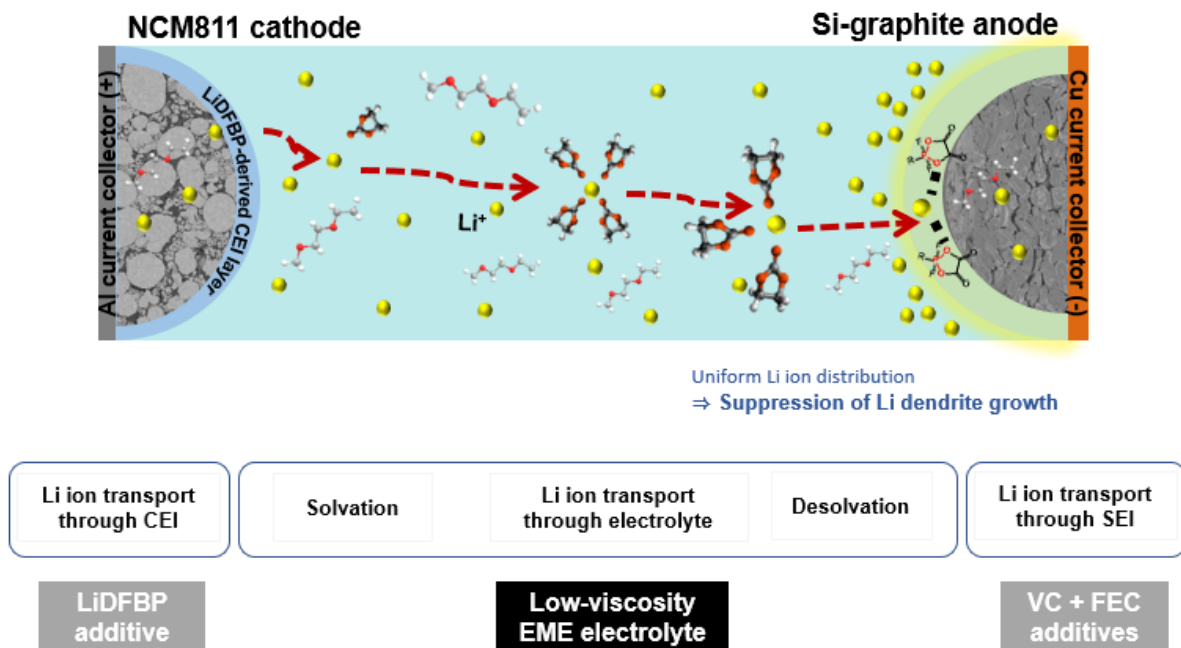


**Figure 15.** Schematic illustration of concentration gradient of Li ion in electrolyte when starting charge with high current density.

## 2. Experimental

### 2.1. Preparation of the electrodes and electrolytes

In this study, a  $\text{LiNi}_{0.8}\text{Co}_{0.1}\text{Mn}_{0.1}\text{O}_2$  (NCM, mixed with large and small particles) cathode and a SiC containing graphite anode were utilized for full cells. Cathodes was composed of  $\text{LiNi}_{0.8}\text{Co}_{0.1}\text{Mn}_{0.1}\text{O}_2$ , conducting material and polyvinylidene fluoride (PVDF) dissolved in N-methyl-2-pyrrolidone (NMP) as an active material, conducting material and a binder (95.8/2/2.2 wt%), respectively. The mass loading of the cathode was  $20.5 \text{ mg/cm}^2$ . The anode was fabricated by mixing 96/1/3 wt% of SiC containing graphite, conducting material and binder dissolved in deionized water. The mass loading of anode was  $10.9 \text{ mg/cm}^2$ . Polyethylene film coated with aluminum oxide ( $\text{Al}_2\text{O}_3$ ) was used as a separator. The thickness was  $15.1 \mu\text{m}$  and porosity was 49.2%.

The baseline electrolyte is composed of 1M lithium hexafluoro phosphate ( $\text{LiPF}_6$ ) dissolved in a solvent mixture of ethylene carbonate (EC), diethyl carbonate (DEC), and ethyl methyl carbonate (EMC) with a 25:30:45 volume ratio. Vinyl carbonate (VC, Enchem Co., Ltd) and fluoroethylene carbonate (FEC, Enchem Co., Ltd) were used as additives to organize an effective SEI layer on the anodes. To discuss the effect of solvent, 30 vol.% of 1-ethoxy-2-methoxy ethane (EME) was added instead of DEC in the baseline electrolyte. Moreover, lithium difluoro(bisoxalato) phosphate ( $\text{LiDFBP}$ , Chunbo) was included as an additive in EC/EME/EMC (25/30/45 vol.%) with 1M lithium hexafluoro phosphate ( $\text{LiPF}_6$ ). The water content in the electrolytes was removed from calcium hydride ( $\text{CaH}_2$ ) by stirring an hour.

Electrolyte	Composition
Carbonate	1M $\text{LiPF}_6$ in EC/EMC/DEC (25/45/30 vol%) + 1wt% VC +3wt% FEC
EME	1M $\text{LiPF}_6$ in EC/EMC/EME (25/45/30 vol%) + 1wt% VC +3wt% FEC
EME + $\text{LiDFBP}$	EME + 1.5 wt% $\text{LiDFBP}$

**Table 2.** Composition of electrolytes.

## 2.2. Electrochemical measurements

NCM cathode and SiC containing graphite anode were used for the 2032 coin cells. The coin cells were assembled in an Ar-filled glove box. A half cell was composed of NCM cathode and Li metal electrode. After the aging process, 1 hour at 45 °C and 20 hours at 25 °C, the electrochemical performance of the full cells was carried out on a computer-controlled battery testing equipment (WonATech WBCS 3000). Full cells were galvanostatically precycled twice between 2.5V and 4.2V vs. Li/Li<sup>+</sup> at 25°C at a fixed C rate (C/10), then the constant voltage was applied until the current was below C/20. The dQ/dV graphs were acquired by computing the differential capacity versus the potential of cells during precycles. Stability of electrolyte on the cathode was examined by a floating test at 25°C, in which 2032 coin type NCM811/Li half cells were charged to 4.3V at a constant current of C/10 and 4.3V was applied for 10 hours at a constant voltage mode. The NCM cathode in the half cell was fabricated with a low loading level of 10.2 mg/cm<sup>2</sup> to avoid the polarization when charging. The anodic stability of the electrolytes was determined by linear sweep voltammetry (LSV) with Li foil at a constant scan rate of 0.5mV s<sup>-1</sup> in the voltage range of 3.0V-5.5 V (vs. Li/Li<sup>+</sup>) at 25°C. To gauge the fast charging cycle performance, the full cells were tested between 2.5V and 4.2V at 45°C at a fixed charge C rate (4C) and discharge C rate (1C). It was controlled by time cut off (4C = 15 minutes cut off). In addition, the cells used for the charge rate capability experiments were cycled at 25°C at a fixed discharge C rate (C/10) and a variety of charge C rates (C/2, 1C, 2C, 3C, C/2).

NCM811/gra-SiC pouch-type full cells were assembled with a separator in a dry room (25°C, humidity <0.6 %). The size of each cathode and anode is 2\*2.5 (cm<sup>2</sup>) and 2.2\*2.7 (cm<sup>2</sup>) with the corresponding tap, cathode to Al-tap and anode to Ni-tap. The size of the separator is 2.6\*3.0 (cm<sup>2</sup>). All the electrodes are dried with vacuum oven over 10 hours at 110°C before assembling pouch. The pouch was assembled with the same amount of electrolyte, 0.2g. After the aging process, the pouch type full cells were precycled twice between 2.5V and 4.2V at 25°C at a current of C/10. At the first cycle of precycling, after 2 hours of charging, stop charging and cut off the gas room of the pouch cell to degassing of the cell by decomposed electrolyte, forming SEI layer. After sealing the pouch with vacuum sealing machine (AZC-010, airzero, INTRISE), the remaining precycle process kept going. The size of the pouch is 4\*5 (cm<sup>2</sup>).

### 2.3. Characterization

EUTECH CON 150 conductivity meter and Brookfield viscometer were used to measure ionic conductivity and viscosity of electrolytes. Wettability of electrolytes was examined by contact angle measurements on the NCM811 cathode using a Phoenix 300. A 10  $\mu\text{L}$  electrolyte was dropped to photograph all snapshots after dropping within 2s. The electrochemical impedance spectroscopy (EIS) measurements for full cells were conducted by AC impedance analysis using an IVIUM frequency response analyzer at SOC of 0%. The frequency range was between 1MHz and 10mHz. The potentiostatic signal amplitude was 5mV.

To examine the volatility of EME and Carbonate, thermogravimetric analysis (TGA) was conducted. Each electrolyte was heated from room temperature to 300°C with a heating rate of 5°C/min. Pouch swelling test was utilized to examine gas evolution of EME. After two precycles, pouch type full cells were charged to 4.2V and then stored at 45°C and 60°C. Thickness of stored pouch type full cells were measured at the same time every day. For accurate measurement, acrylic plates and micrometer were used.

To investigate the effect of EME and LiDFBP-derived CEI layer, the transition metal dissolution is gauged by inductively coupled plasma-optical emission spectrometer (ICP-OES). Delithiated cathodes were stored in the same amount of electrolyte (2g). The samples were kept for 7 days at 45 °C with aluminum pouch sealing of PE vial. To compare the amount of HF with each electrolytes, the samples were kept for 20 days at 45 °C with aluminum pouch sealing of PE vial. Then,  $^{19}\text{F}$  NMR spectra were recorded with AVANCE 3 HD 400 MHz FT-NMR (Bruker) with THF-d8 as a solvent.

The electrochemical window of the organic solvent and additives, the molecule optimization of geometry was obtained using density functional theory with Gaussian 09 at B3LYP/6-31+G level.

After precycling and cycling, the cells were disassembled in a glove box to obtain the electrodes. Then, the electrodes were rinsed in DMC to remove the residual electrolyte. After sufficiently volatilizing the DMC at room temperature, each sample was sealed in an aluminum pouch to prevent contamination. The electrodes were used for surface chemistry and cross-section.

To investigate the degree of charge state, the X-ray diffraction (XRD) patterns of charged cathodes in different electrolytes were acquired by using a Rigaku D/MAX 2500V/PC X-ray diffractometer equipped with a Cu Ka radiation source ( $\lambda = 1.54184 \text{ \AA}$ ). The samples were scanned over the  $2\theta$  range of 10-80° at 2°/min.

The surface composition was studied by ex-situ X-ray photoelectron spectroscopy (XPS, Kratos Axis Ultra spectrometer, Al Ka radiation,  $h\nu = 1486.6 \text{ eV}$ ) under high vacuum. The cross-sectional images of the electrodes obtained after the cycling test were acquired with scanning electron microscope (SEM, Verios 460, FEI) under high-vacuum environment after the cross section was prepared by ion milling system (IM4000, Hitachi) that utilizes an Ar-ion beam.

### 3. Result and discussion

#### 3.1. Effect of low viscous EME solvent

Conventional low-viscosity solvents have the disadvantage of causing pouch swelling issues due to their high volatility. Low-viscosity EME has the advantage of boiling point of 102°C, which is higher than conventional low-viscosity solvents. Therefore, to examine the volatility of EME, the TGA of the electrolytes containing lithium salt and solvents without any additives are performed. Unlike conventional low-viscosity solvents like DMC, EME w/o additive takes longer to evaporate than Carbonate w/o additive (**Figure 16**). The result implies that the EME shows low volatility. Pouch swelling tests are conducted to confirm the amount of gas generated in the cell. [28] EME electrolyte shows much less gas evolution than DMC at 60°C (**Figure 17**). In addition, the pouch type cell with EME electrolyte showed a thickness change similar to that of carbonate. It indicates that less gas is generated at a level similar to that of commercially used carbonate. Therefore, the introduction of a low-viscosity solvent EME with a high boiling point has an advantage of improving safety compared to a conventional low-viscosity solvent.

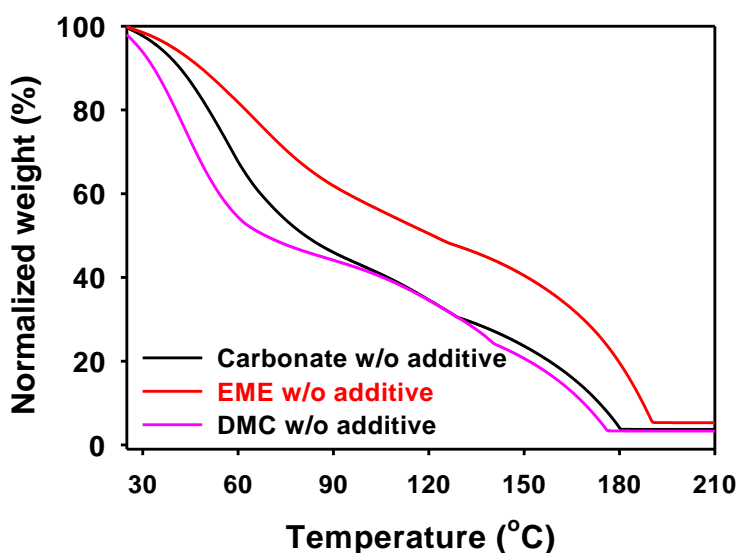


**Figure 16.** TGA of electrolytes containing solvents and lithium salts only without additives.

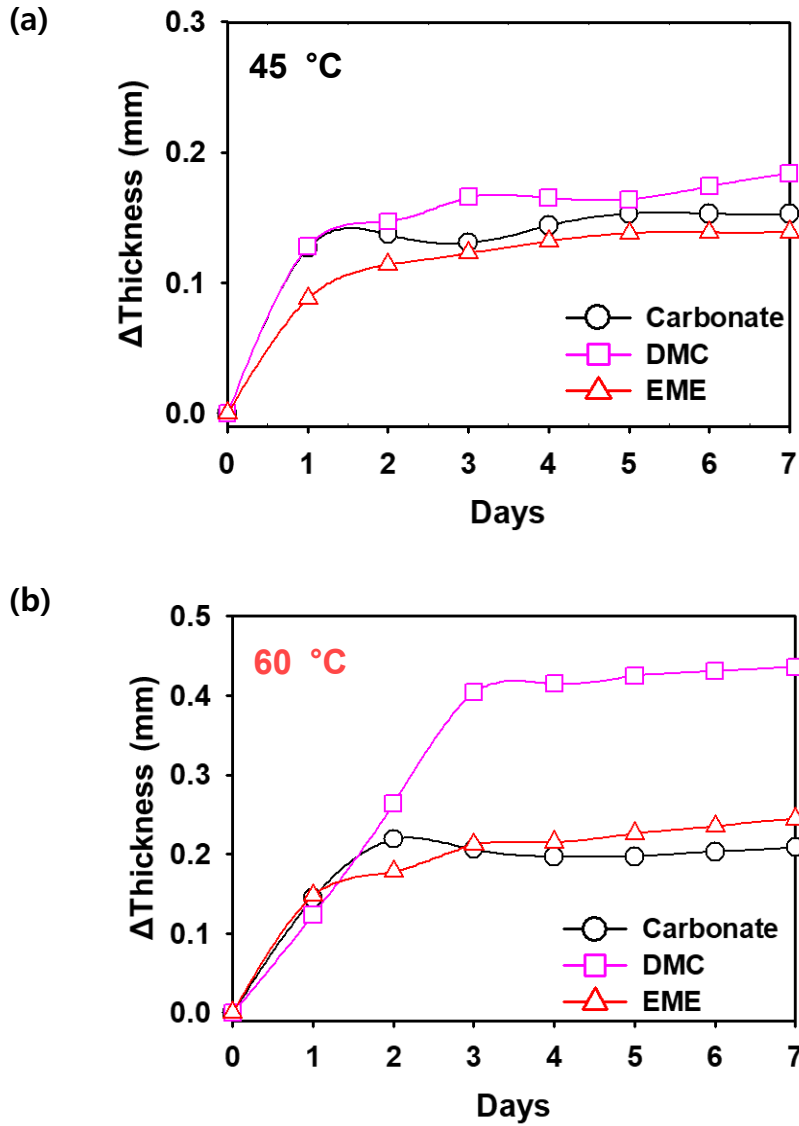


**Figure 17.** (a) Changes in the thickness of the pouch-type full cells stored at 45°C. (b) Changes in the thickness of the pouch-type full cells stored at 60°C.

The ionic conductivity of electrolyte is also one of the most critical factors to decide rate capability. **Figure 18a** shows viscosities and ionic conductivities of Carbonate and EME. The ionic conductivity dramatically increases when EME solvent is used as a cosolvent, while viscosities decreases. High ionic conductivity (12.9 mS/cm) and low viscosity (0.52 cP) of EME solvent implies the fast ion transport. Thus, these values indicate that EME will show improved rate capability.

To realize high-energy-density LIBs, electrolyte penetration toward high-mass-loading electrodes is also crucial. Insufficient wetting of the electrodes leads to decreased active sites of active materials, causing lower capacity. In particular, insufficient wetting on the cathode is more critical on capacity because anode still has a higher capacity and available vacancy sites for the Li ions. Thus, the contact angle measurement is conducted to examine the impregnation characteristic of the electrolytes on the NCM811 cathode with high loading level of 20.5 mg/cm<sup>2</sup>. In **Figure 18b**, the EME electrolyte shows lower contact angle of 18.1° on NCM cathode, while the Carbonate electrolyte represents contact angle of 28.2° on the cathode. The lower contact angle means the better wettability toward the thick electrodes. The result demonstrates that the introduction of low-viscosity EME solvent improves impregnation of electrolyte toward thick electrodes. [29]

To evaluate the impedance and lithium conductivity of EME, AC impedance of NCM811/gra-SiC full cells was obtained by electrochemical impedance spectroscopy (EIS). **Figure 19a** shows the cell impedance of Carbonate and EME after formation cycle. The former semicircle in high frequency range means the SEI resistance, while the latter in low frequency range stands for the Li ions transfer resistance. The introduction of the low-viscosity solvent EME leads to lower interfacial impedance than Carbonate. The decreased charge transport resistance indicates that the low viscosity of EME electrolyte has a positive influence on the Li ions transport. Facile Li ion diffusion leads to an improvement in charge rate capability of full cells with EME. The rate capability performance at various charge current densities shows that the effect of EME in **Figure 19b**. At the 3C of charge state, EME electrolyte delivers shows 68.3% of discharge capacity from 0.5 C-rate, compared to 59.3% of discharge capacity with Carbonate. These results confirm that the EME has low impedance and provides superior lithium conductivity, improving fast charging capability of NCM811/gra-SiC full cells.



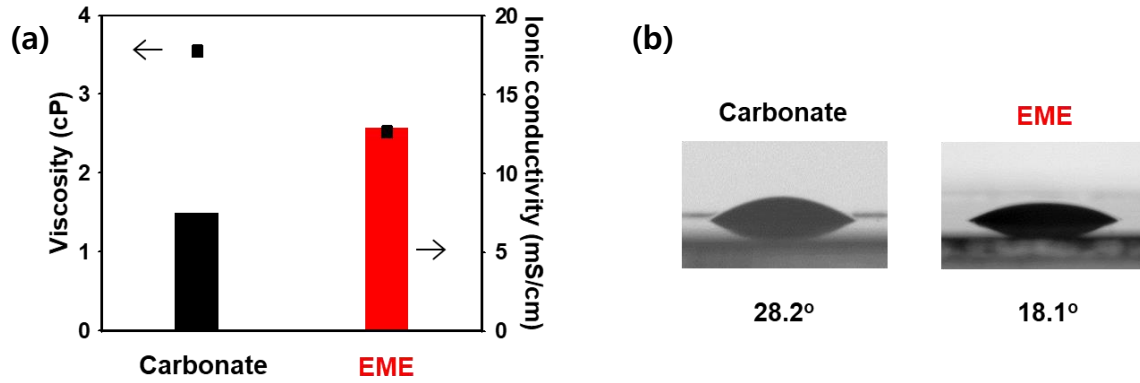


**Figure 18.** (a) Viscosity (points and left side y axis) and Conductivity (bars and right side y axis) values of Carbonate and EME. (b) Photographs of electrolyte's contact angle on NCM811 cathode.

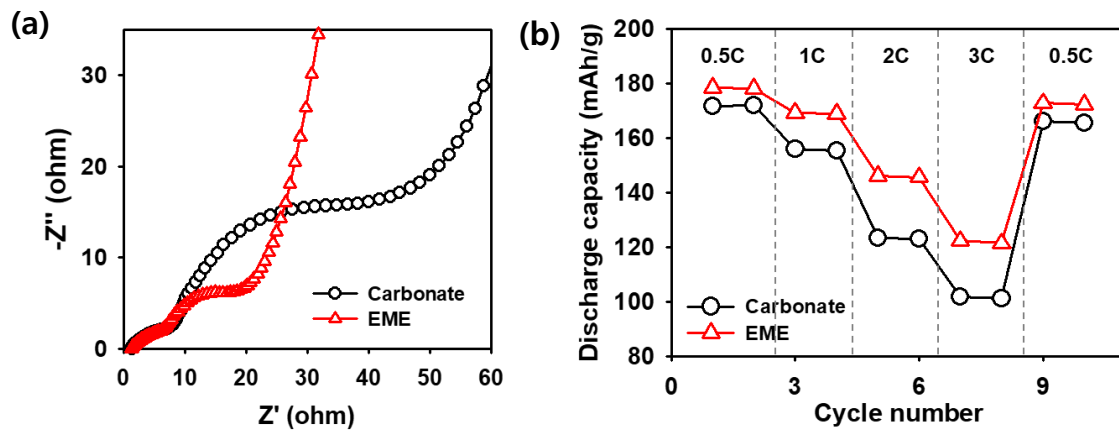


**Figure 19.** (a) The impedances spectra of NCM811/gra-SiC full cells with Carbonate and EME after precycles. (b) Comparison of the charge rate capability of NCM811/gra-SiC full cells with Carbonate and EME.

**Figure 20** shows the XRD patterns of the charged NCM811 cathodes from NCM811/gra-SiC full cells with Carbonate or EME after charging at 4C. Obvious splits of the (108)/(110) peaks imply that the charged NCM811 cathode with EME is more delithiated than that with Carbonate. [30-32] Also, by using EME solvent, the peaks of (107) shift to lower  $2\theta$ -angles. The peak shift indicates an extension in the c axis due to the increasing electrostatic repulsion between the  $(\text{Ni}_{0.8}\text{Co}_{0.1}\text{Mn}_{0.1})\text{O}_2$  sheets during delithiation. The EME electrolyte reveals a superior delithiation ability than the Carbonate electrolyte, enabling facile Li ion diffusion in the primary particles of the cathode.

To confirm voltage stability of CEI layer formed by EME cosolvent on the NCM811 cathode, the electrochemical floating test is conducted at 25°C. (**Figure 21**). All the cells are charged to 4.3V, followed by holding at 4.3V for 10h. The EME electrolyte shows oxidation current similar to that of Carbonate, which implies that the Cathode electrolyte interphase (CEI) formed by EME is as stable as the CEI formed by Carbonate at 25°C.

Linear sweep voltammetry (LSV) was utilized to confirm anodic stability of EME at high temperature (**Figure 22**). The potential scan is carried out from the open circuit voltage to 5.5V. EME electrolyte represents an anodic current at about 4.3 V at 60°C, whereas Carbonate electrolyte generates anodic current at about 4.6 V at 60°C. The LSV result suggests that EME solvent has lower anodic stability at high temperature.

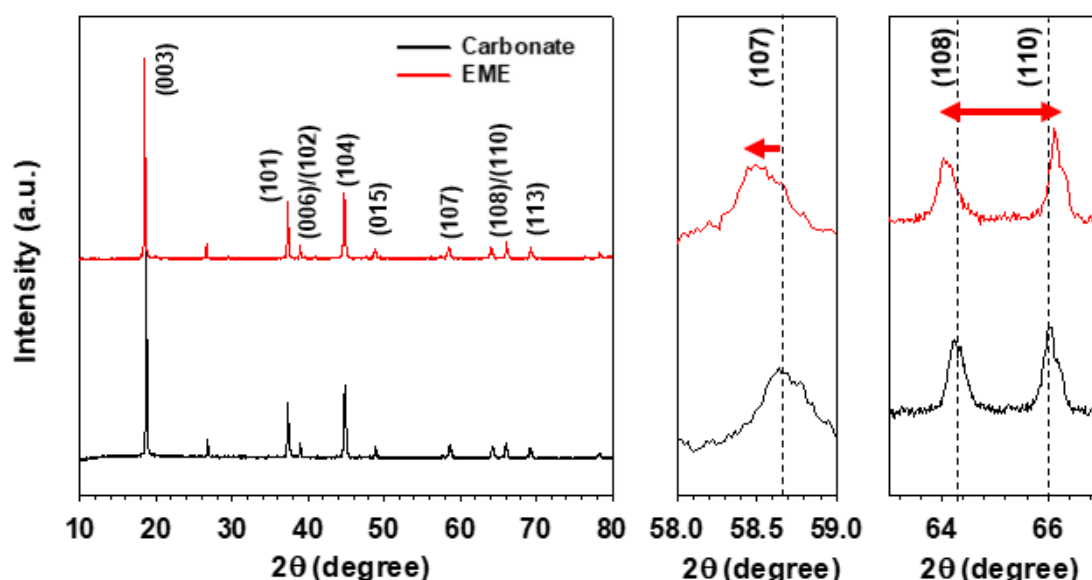


**Figure 20.** XRD patterns of charged NCM811 cathode at 4C-rate after precycles.

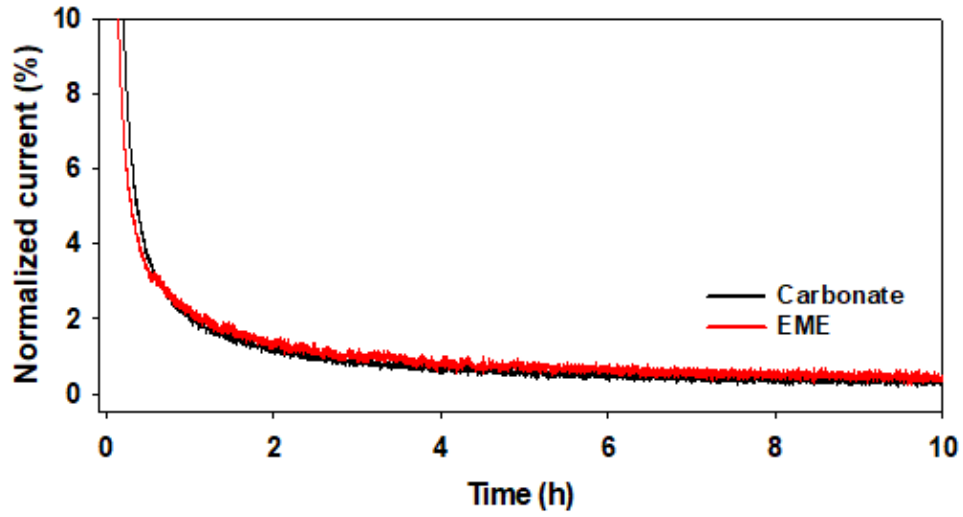


Figure 21. Floating test of NCM811/Li half cells charged 4.3V at 25°C.

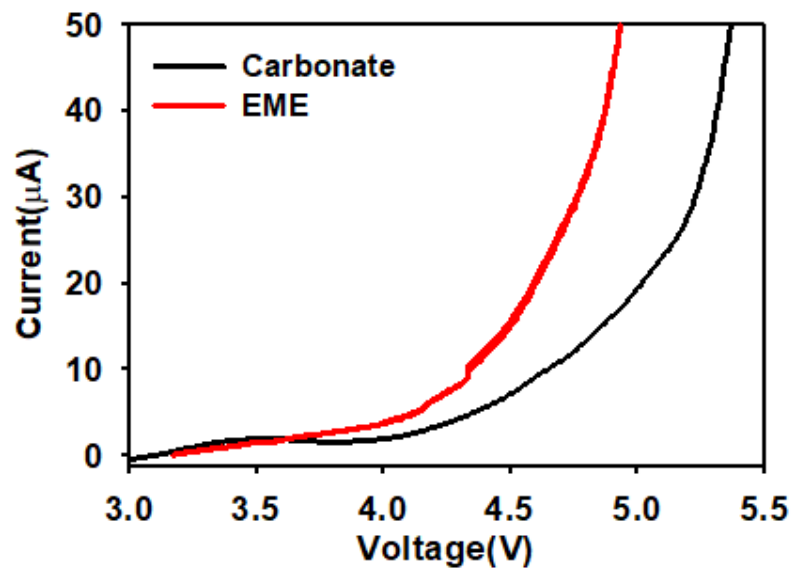
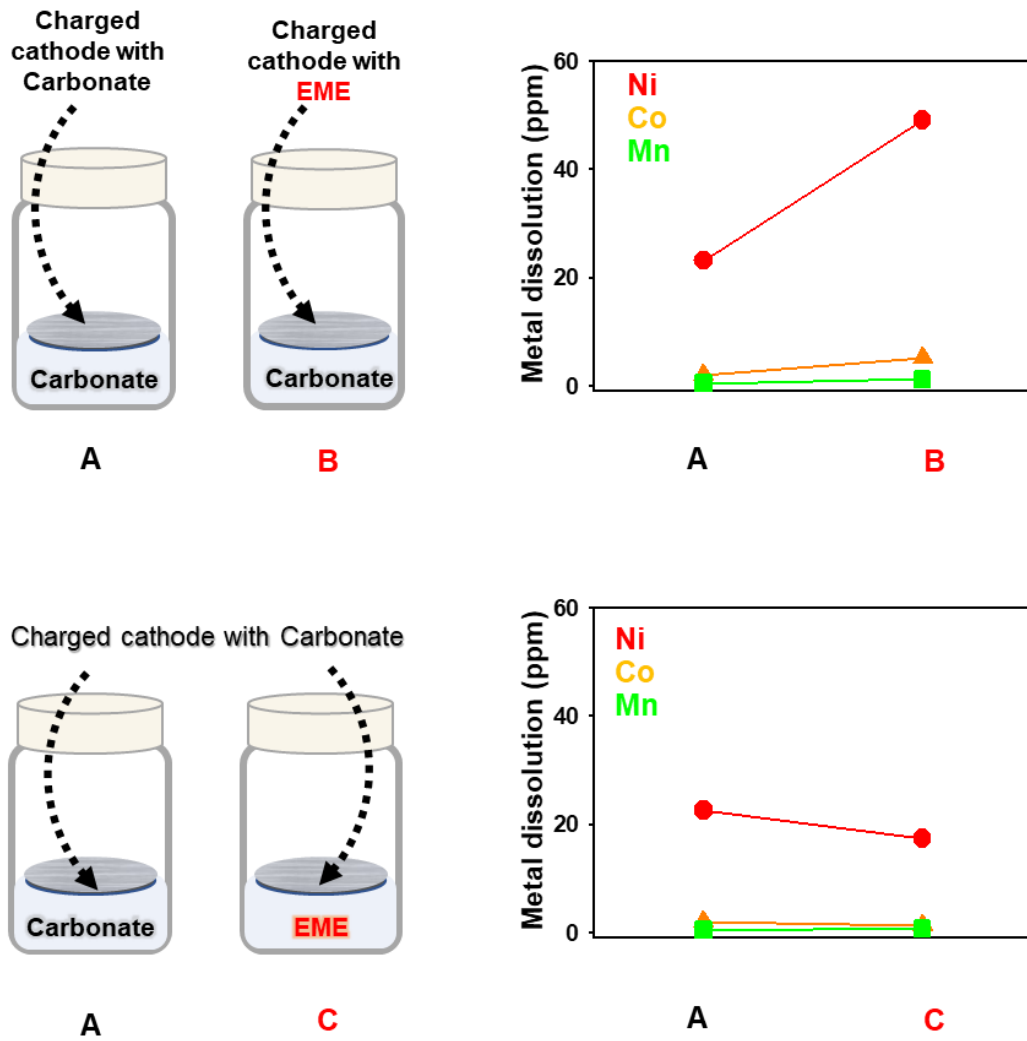


Figure 22. LSV of Carbonate and EME at 60°C.

To examine thermal stability of EME, two type transition metal dissolution tests are conducted. Dissolved transition metal ions are estimated by using an inductively coupled plasma-optical emission spectrometer (ICP-OES) after storage at 45°C for 7 days. [33] First, to investigate the effect of CEI formed by EME on transition metal dissolution at high temperature, transition metal dissolution in the same electrolyte (Carbonate electrolyte) is measured while storing charged cathodes with different CEI layer on the surface, for 7 days at 45 °C. The sample B shows a much higher content of transition metals such as Ni<sup>3+</sup>, Ni<sup>4+</sup>, Co<sup>4+</sup>, and Mn<sup>4+</sup> than sample A. Fully delithiated cathodes without a proper CEI tend to release transition metal ions into the electrolyte. The result demonstrates that CEI formed by EME cosolvent is unstable at high temperature, not inhibiting transition metal dissolution. Then, in order to examine the effect of bulk characteristics of EME on transition metal dissolution at high temperature, charged cathodes with Carbonate are stored in different electrolytes. After storage at 45°C for 7 days, sample C has a similar amount of metal dissolution to sample A. These results indicate that the EME electrolyte itself does not dissolve transition metals more, but the film formed by EME cannot prevent transition metal dissolution due to its thermal instability.

<sup>19</sup>F NMR spectroscopy is conducted to confirm the influence of EME on HF generation. HF generated by hydrolysis reactions of LiPF<sub>6</sub> salt can give rise to dissolution of transition metal ions from the NCM811 positive electrode. [34] Carbonate and EME electrolytes are stored at 45°C for 20days. After storage, the changes in the electrolytes were monitored by <sup>19</sup>F NMR spectroscopy. The peaks near -84 and -86 ppm could be attributable to PO<sub>2</sub>F<sub>2</sub><sup>-</sup>. The characteristic HF peak at -194 ppm appears after storage. The peaks are generated by hydrolysis reactions of LiPF<sub>6</sub> salt (**Figure 24**). EME shows similar the relative intensity and the volume ratio of HF and PO<sub>2</sub>F<sub>2</sub><sup>-</sup> to Carbonate (**Figure 25**). It is clear that EME does not accelerate hydrolysis reactions of LiPF<sub>6</sub> and HF generation.

The transition metal dissolution tests and the <sup>19</sup>F NMR spectra show that the film formed by EME electrolyte is unstable at high temperature, which is the main cause of transition metal dissolution from the cathode. Therefore, it is necessary to introduce an additive to make up a stable and uniform film on the electrodes.



**Figure 23.** Transition metal dissolution degree analyzed by inductively coupled plasma (ICP). Charged cathodes with Carbonate were stored in (a) Carbonate electrolyte and (b) EME electrolyte. (c) Charged cathode with EME.

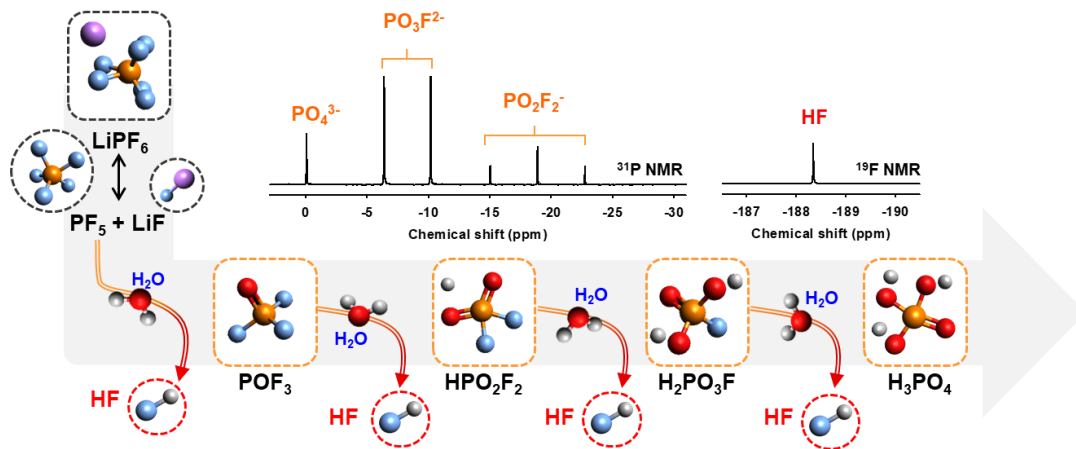


Figure 24. Hydrolysis reactions of  $\text{LiPF}_6$  salt in the presence of water in the cell. [34]

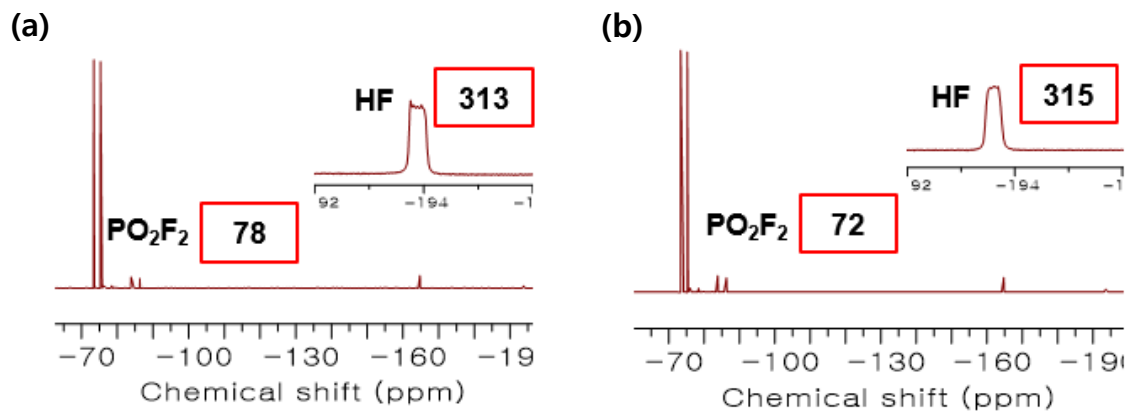
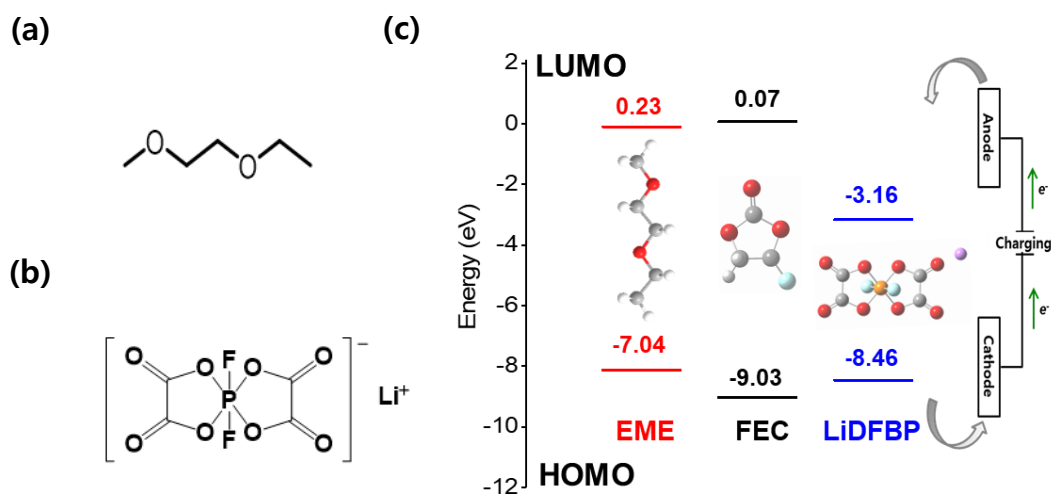


Figure 25.  $^{19}\text{F}$  NMR spectra with (a) Carbonate (b) EME storing for 20 days at 45 °C.

### 3.2. Introduction of LiDFBP additive to complement EME solvent

To prevent the decomposition of EME solvent and complement its unstable SEI, Lithium difluoro(bisoxalato) phosphate (LiDFBP) is introduced. LiDFBP additive can undergo reductive decomposition because it has lower Lowest Unoccupied Molecular Orbital (LUMO) energy level than EME (**Figure 26**). Since LUMO energy level of LiDFBP (-3.16 eV) is lower than that of EME (0.23 eV) and FEC (0.07 eV), LiDFBP is easier to lose electrons compared to EME and FEC while lithiation process occurs. During reductive decomposition, LiDFBP can form a passivation film on the electrode. This SEI protects severe decomposition of EME solvent.

**Figure 27** shows the plots of  $dQ/dV$  vs voltage during the initial charge process for the NCM811/graphite full cells without and with additives. The peak at 2.6V is due to reductive decomposition of EME solvent. By adding LiDFBP additive, the peak corresponding to decomposition of EME disappears. Also, the EME + LiDFBP electrolyte shows the reductive decomposition peak at 1.7V. This result implies that LiDFBP, which first decomposes at 1.7V, inhibits the decomposition of EME solvent. In addition, the LiDFBP effectively improves anodic stability of the electrolyte containing EME solvent at high temperature as shown in **Figure 28**.



**Figure 26.** Chemical structure of (a) 1-ethoxy-2-methoxy ethane (EME) and (b) Lithium difluoro(bisoxalato) phosphate (LiDFBP). (c) HOMO and LUMO energy level of EME, FEC, and LiDFBP.

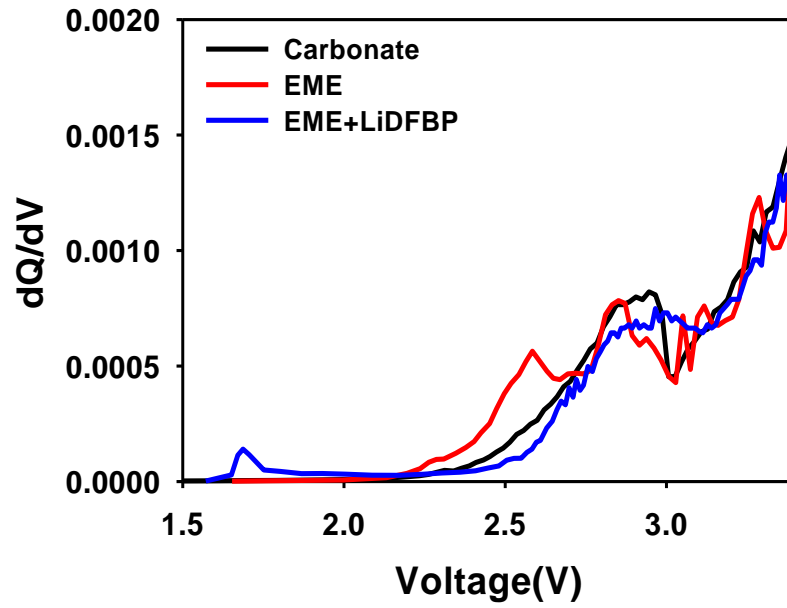


**Figure 27.** dQ/dV plot of NCM811/gra-SiC full cells with Carbonate, EME, and EME + LiDFBP during first lithiation.

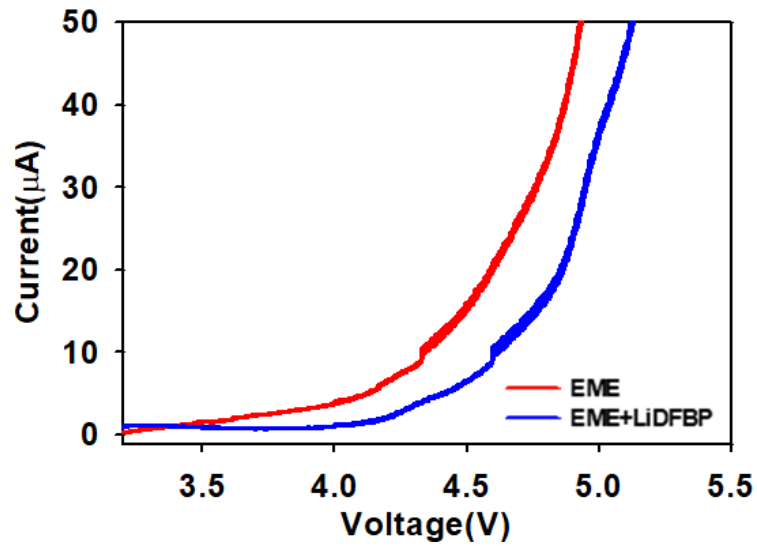


**Figure 28.** LSV of EME and EME + LiDFBP at 60°C.



**Figure 29a** shows the cycling stability of NCM811/gra-SiC anode full cells with Carbonate, EME, and EME + LiDFBP at 45°C. The full cells are cycled 50 times in the voltage range of 4.2V – 2.5V. Because low viscosity of EME solvent enabled facile delithiation, the first discharge capacity of the full cell with EME is higher than Carbonate. However, the cell with EME electrolyte undergoes severe discharge capacity fading from about 40<sup>th</sup> cycle due to continuous decomposition of EME. 72.2% and 56.1% of discharge capacity retention are obtained after 50 cycles by using Carbonate and EME, respectively. With 1.5wt% LiDFBP, cycle performance is significantly enhanced. 84.6% of the discharge capacity retention was obtained after 50 cycles. The initial discharge capacity of EME +LiDFBP is slightly low due to the slightly larger interfacial resistance. In addition, EME + LiDFBP maintained high coulombic efficiency after 40 cycles by suppressing decomposition of EME solvent (**Figure 29b**). The expected reason for this superior performance of EME + LiDFBP is the synergistic effect of low-viscosity EME solvent and stable film forming LiDFBP additive. Low viscous solvent enables facile Li ion diffusion, increasing charge capacity at a rate of 4C. LiDFBP additive forms stable and uniform film on the cathode and anode, preventing deterioration of active materials and electrolyte decomposition.

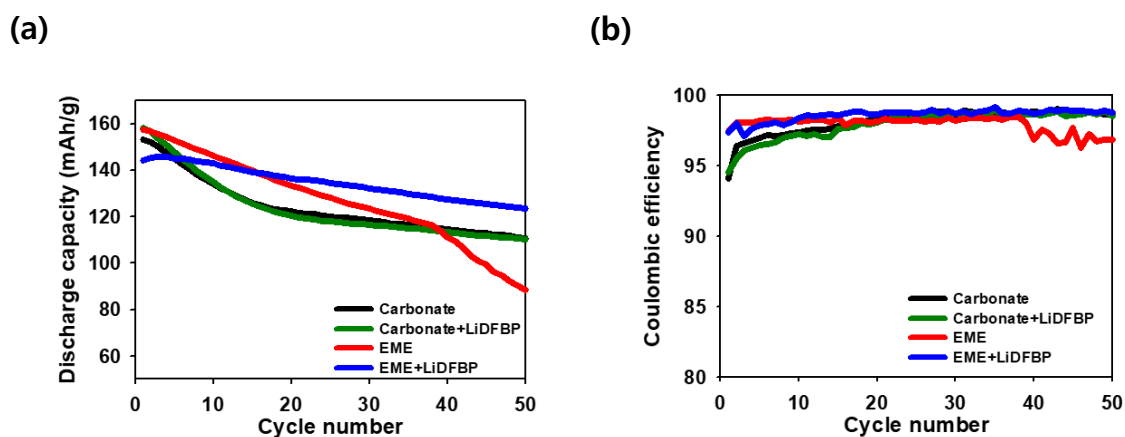
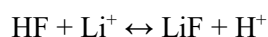


**Figure 29.** Electrochemical performance of NCM811/gra-SiC full cells with Carbonate, Carbonate+LiDFBP, EME, and EME + LiDFBP. The cells were cycled with 4C charge and 1C discharge at 45°C. (a) Discharge capacity versus cycle number. (c) Coulombic efficiency.

To evaluate the effect of LiDFBP additive on the cathode, **Figure 29** shows the O 1s and F 1s spectra of NCM811 cathodes acquired from NCM811/gra-SiC full cells after two precycles. In the O 1s spectra, the fraction of C=O at 531.8 eV increased from 68.3% to 74.6% by using LiDFBP additive. Carbonate (C=O) species are fabricated by oxidative decomposition of LiDFBP at the NCM811 cathode (**Figure 30**). [26, 36]

In addition, the NCM811 cathode with EME + LiDFBP reveals a increase in the peak intensity assigned to C-F at 687.7 eV, relative to the cathode with EME. The C-F peak corresponds to the PVDF binders on the cathodes. Thus, the increase of the C-F peak intensity indicates that LiDFBP prevents the electrolyte decomposition and forms a thin surface film. In other words, the increase of the C-F peak intensity is because the thin surface film formed by LiDFBP additive does not block the F signal from the cathode, unlike EME. F 1s spectra also shows drastically reduced the peak of LiF at 684.9 eV. The decrease in the peak intensity implies that the LiDFBP-derived CEI prevents the oxidation of LiPF<sub>6</sub> salt on the cathode and HF attack. LiPF<sub>6</sub> salt can form LiF and HF (**Figure 24**). The formation process of LiF and HF can be described by following chemical equation.



To confirm whether the LiDFBP additive protects NCM811 cathodes during cycling, the SEM analysis of the NCM811 cathodes after 50cycles at 45°C was performed. **Figure 31** shows the cross-sectional back-scatter electron (BSE) images of cycled NCM811 cathodes retrieved from the cells with the EME and the EME + LiDFBP electrolyte. During fast charging at a rate of 4C, microcracks propagate inside secondary NCM811 particles as the layered structure of the cathode undergoes drastic volume changes. [35] The intergranular cracking of NCM cathodes deteriorates the cathode's ability to maintain its original capacity. The cathode cycled with EME electrolyte suffers from severe microcracks, while the cathode cycled with EME + LiDFBP has much less secondary particle breakdown. Because the CEI formed by decomposition of EME solvent is electrochemically and thermally unstable, the CEI cannot protect active cathode materials from HF produced by hydrolysis of LiPF<sub>6</sub> at high temperature, allowing the microcracks to propagate. By introducing LiDFBP which forms a stable film, the formation of microcracks is mitigated because active materials are effectively protected from HF attack. As the LiDFBP-derived film prevents propagation of microcracks, metal dissolution such as Ni, Mn, and Co is also inhibited.

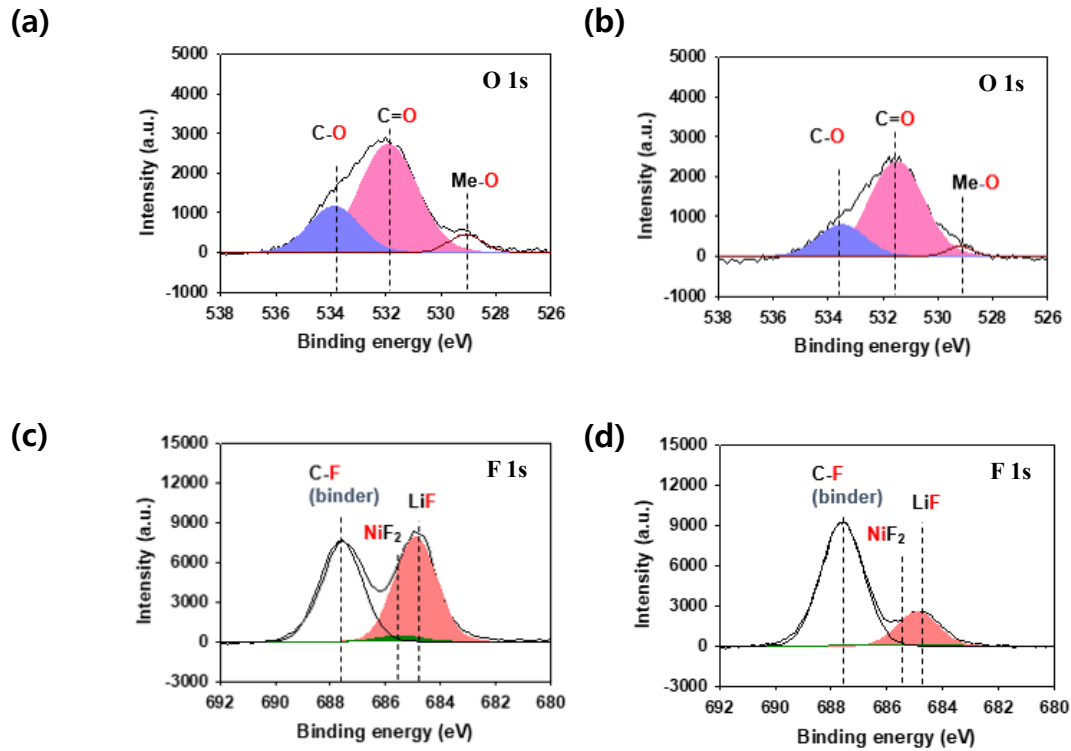


**Figure 29.** O 1s and F 1s XPS spectra of NCM811 cathodes from NCM811/gra-SiC full cells after formation cycle (EME : (a), (c); and EME + LiDFBP : (b), (d)).

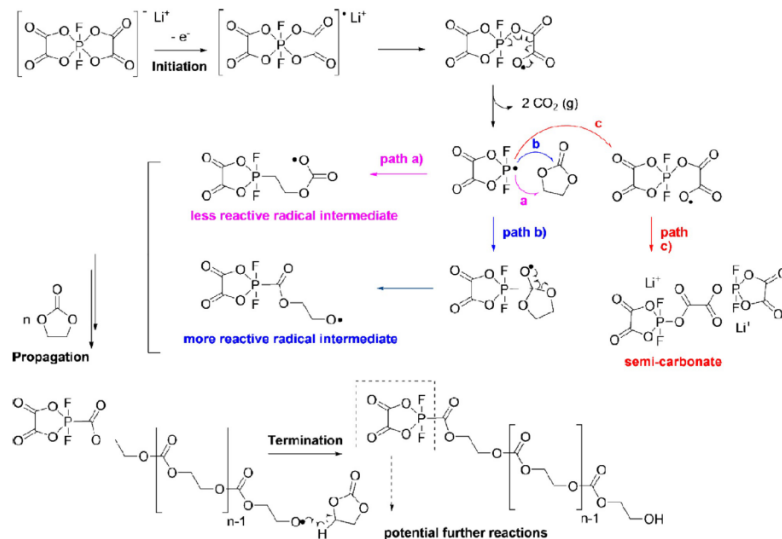


**Figure 30.** Possible mechanisms for SEI formation by the oxidative decomposition of LiDFBP.

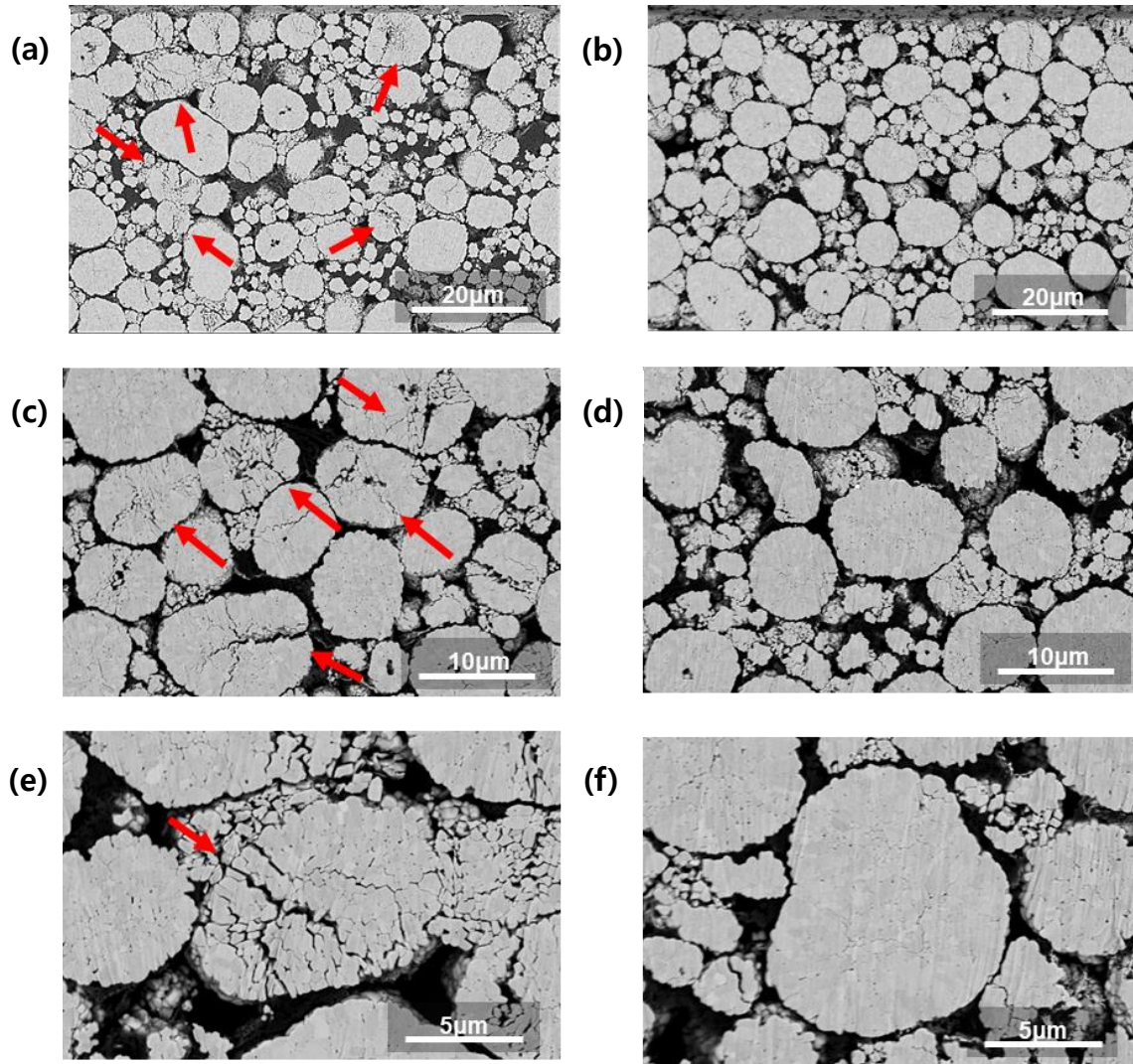


**Figure 31.** BSE images from the cross-sectional SEM of NCM811 cathodes (a), (c), (e) cycled with EME and (b), (d), (f) cycled with EME + LiDFBP. Red arrows indicate microcracks of the cathode.

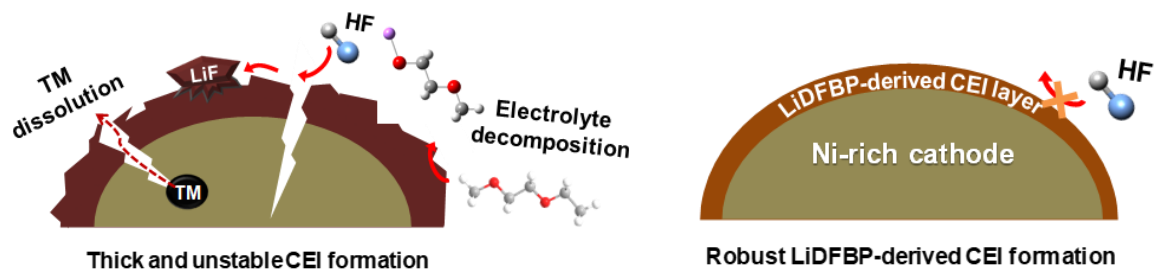


**Figure 32.** Schematic illustration of effects of LiDFBP-derived CEI on deterioration of the NCM811 cathode.

For verification of the manifestation of the influence of EME and LiDFBP on the transition metal dissolution, charged NCM811 cathodes after formation cycles in the different electrolytes were immersed in the respective electrolytes and stored at 45°C for 7 days (**Figure 33a**). The contents of Ni, Co, and Mn ions in the EME electrolyte after storage were 31.3, 3.7, and 0.4 ppm, respectively (**Figure 33b**). The considerable amount of dissolved transition metal ions compared to Carbonate is due to the unstable CEI layer which cannot shield the NCM811 from acidic species. Unveiling of the active material caused by HF attack exposes strongly oxidizing Ni<sup>4+</sup> to the electrolyte. While Ni<sup>4+</sup> species attain electrons from the electrolyte at the surface of the cathode, electrolyte loses electrons, continuously decomposing. As a result, tetravalent Ni ions in the charged NCM cathode are reduced to divalent Ni ions. **Figure 33c** shows the process of transition metal dissolution, migration to the anode, and deposition on the anode. The solubilized divalent Ni ions migrate to the anode and are deposited on the anode. The divalent nickel ions amalgamate with HF, forming resistive NiF<sub>2</sub> compound. Moreover, transition metal deposition results in Li extraction from the lithiated anode, diminishing the reversible capacity. The resistive metal fluorides like NiF<sub>2</sub> can also interrupt the lithium intercalation into the gra-SiC anode, deteriorating rate capability and cycle stability.

The addition of LiDFBP represents much less metal dissolution, compared to EME. This finding indicates that surface chemistry of the cathode changed by LiDFBP improves thermal stability to hinder the oxidation of electrolyte and HF-induced dissolution of metal ions. To verify the effect of LiDFBP on deposition of NiF<sub>2</sub> in the cell, Ni 2p spectra was obtained from cathodes and anodes cycled with and without LiDFBP after 50 cycles at 45°C. In the case of the cathode, as LiDFBP-derived CEI layer hampers the generation of microcracks, the peak intensity of NiF<sub>2</sub> is lower than EME (**Figure 33d**). **Figure 33e** reveals that the peak intensity of deposited NiF<sub>2</sub> on the anode is also low. [36] The Ni 2p spectra correspond to the above result of the transition metal dissolution test. The passivation layer formed by LiDFBP additive lowers the amount of deposited metal ions on the anode, suppressing dissolution of metal ions from the layered metal oxide. The reduction of resistive NiF<sub>2</sub> leads to low interfacial impedance. Consequently, LiDFBP upgraded cycle retention of the full cells with EME + LiDFBP at high temperature.

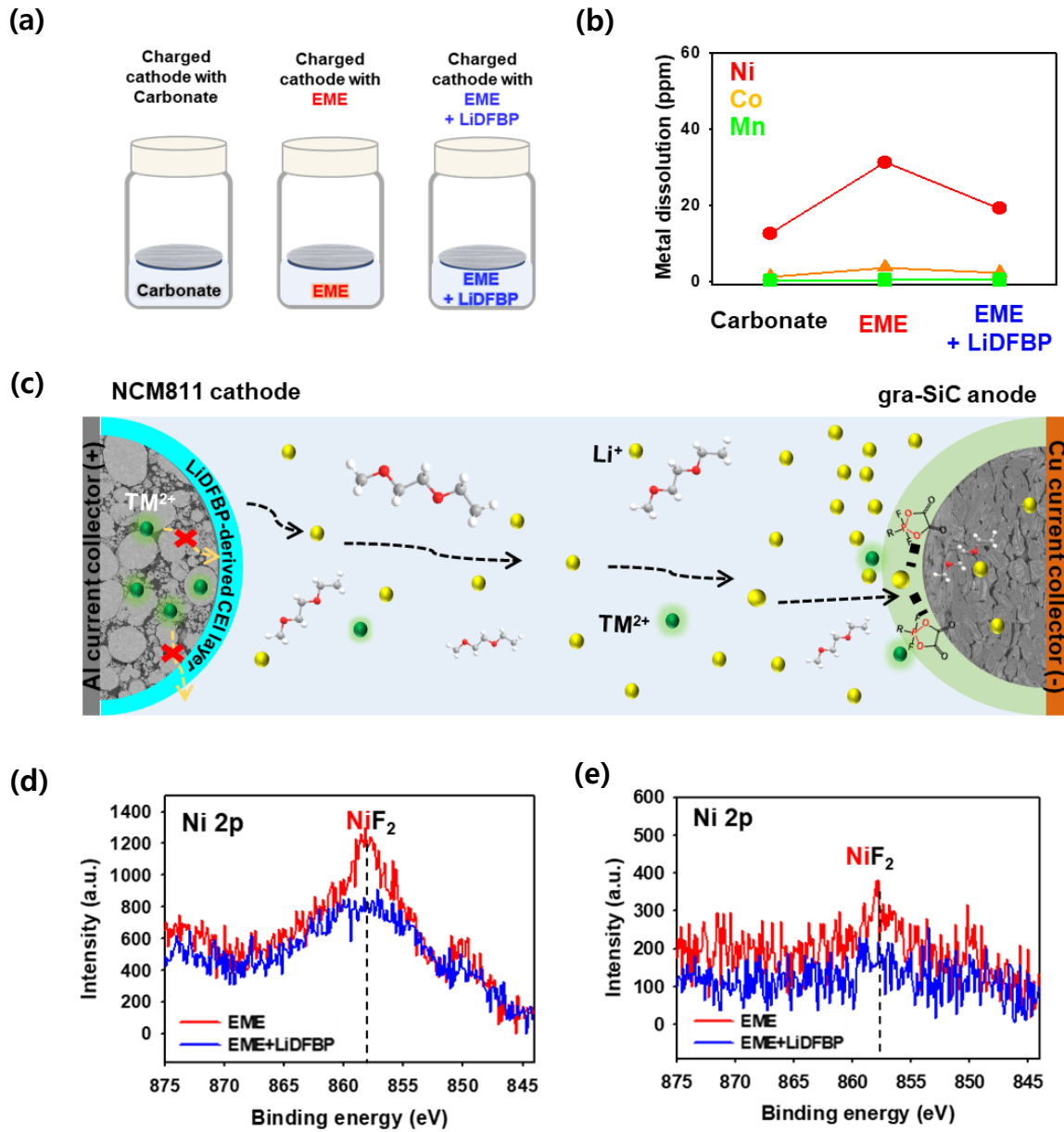


**Figure 33.** (a) Schematic illustration of transition metal dissolution test. (b) Transition metal dissolution degree analyzed by inductively coupled plasma (ICP). (c) Schematic illustration of beneficial effects of LiDFBP additive on transition metal dissolution, migration, and deposition processes. (d) Ni 2p XPS spectra of NCM811 cathode extracted from NCM811/gra-SiC full cells after 50 cycles at 45°C. (e) Ni 2p spectra of gra-SiC anode extracted from NCM811/gra-SiC full cells after 50 cycles at 45°C.

**Figure 34** shows the C 1s, F 1s, and O 1s XPS spectra for the gra-SiC anodes after precycle with Carbonate, EME and EME + LiDFBP. As presented on the C 1s spectra, the anodes with EME appears a reduction in the peak intensity attributable to C-C at 284.8 eV, relative to the anode with Carbonate (**Figure 34a**). The C-C peak corresponds to the graphite. Thus, the decrease in the C-C peak intensity indicates that the SEI layer formed by EME electrolyte is thick. In other words, the decrease in the C-C peak intensity is because thick surface film formed by LiDFBP additive blocks the C signal. On the other hand, with EME + LiDFBP electrolyte, the peak intensity assigned to the C-C is the lowest among three electrolytes. In F 1s spectra, the peak at 684.9 eV and the peak at 686 eV indicates LiF and NiF<sub>2</sub>, respectively. By replacing Carbonate with EME, the peak intensity of LiF and NiF<sub>2</sub> increases (**Figure 34b**). The result indicates that the SEI layer formed by EME electrolyte was not able to protect cathode from HF attack, corresponding to the result of the transition metal test. In addition, HF reacts with active Li ions, forming LiF. [37] On the other hand, by using LiDFBP additive, the peak intensity of resistive LiF and NiF<sub>2</sub> decreases. LiDFBP successfully protects the anode from HF attack and prevented metal ions dissolution of the NCM cathode. The reduction of resistive LiF and NiF<sub>2</sub> leads to improved fast charging capability. In the O 1s spectra, with EME electrolyte, the peak intensity of lithium alkoxide (ROLi) is the highest among three electrolytes (**Figure 34c**). [38] Lithium alkoxides (ROLi) are easily produced by decomposition of EME solvent as shown in **Figure 37**. With the LiDFBP containing electrolyte, the ROLi peak intensity decreased, compared to EME electrolyte. This is because LiDFBP decomposed prior to EME solvent during first charging and prevented the continuous decomposition of EME solvent.

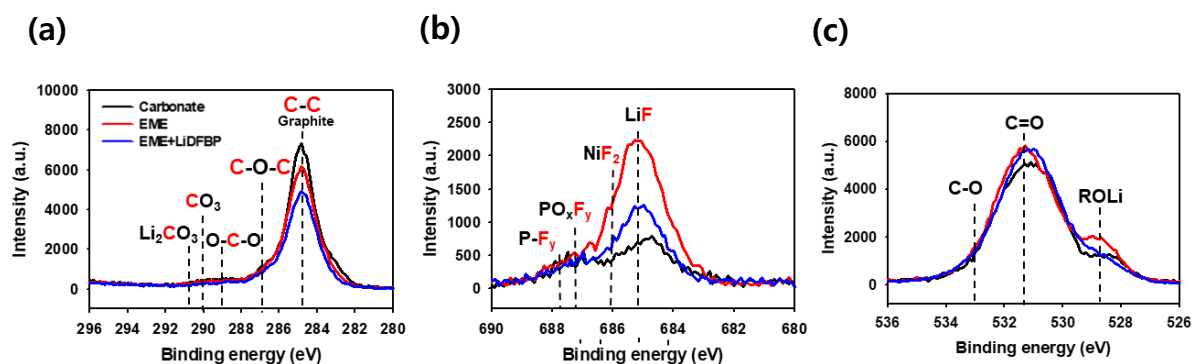


**Figure 34.** (a) C 1s, (b) F 1s, and (c) O 1s XPS spectra of NCM811 cathodes from NCM811/gra-SiC full cells after precycle.

The SEM images of the cycled gra-SiC anodes are shown in **Figure 35**. After 50cycles with 4C charge and 1C discharge at 45°C, the surface of gra-SiC anode was observed to identify the deterioration of the particles in each electrolyte composition. The surface, used with the Carbonate electrolyte, is covered with byproducts. In the case of EME, anode deterioration is more severe, making it difficult to identify its origin shape (**Figure 35b, e**). This is probably because the surface film formed by EME electrolyte is not thermally stable enough to maintain its structure at 45°C. EME solvent might have decomposed continuously during cycling at high temperature because the unstable and non-uniform film cannot protect the anode from electrolyte decomposition. The thick byproducts layer can act as a resistive layer, causing irreversible loss of capacity. Also, unlike Carbonate electrolyte, dendritic Li were deposited on the gra-SiC anode. [39, 40] Due to resistive SEI species like metal fluorides, many Li ions might be not able to intercalate into the anode with 4C charge. In case of EME + LiDFBP electrolyte, smooth surface of graphite particles is obtained. It indicates that the charging and discharging process were carried out with ionic SEI layer on the surface which effectively pass through Li-ion. The cycled anode with EME + LiDFBP electrolyte has little byproducts and lithium dendrites (**Figure 35c**). The cross-sectional images of the cycled gra-SiC anode with EME + LiDFBP reveals that LiDFBP-derived SEI layer is thin and uniform even after 50 cycles at 45°C (**Figure 35f**).

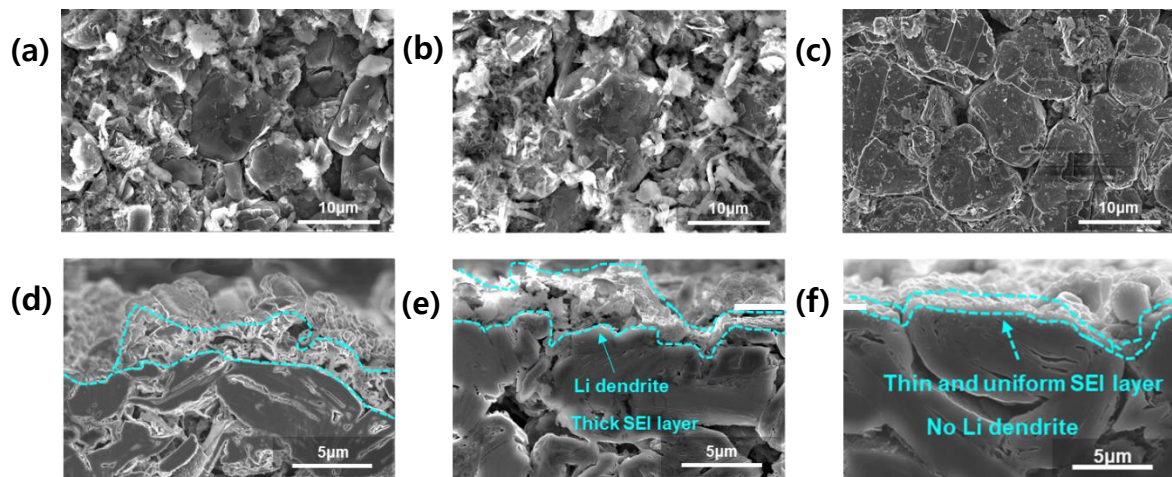


**Figure 35.** The top-view and the cross-sectional SEM images of gra-SiC anode obtained from the NCM811/gra-SiC full cell with (a), (d) Carbonate , (b), (e) EME, and (c), (f) EME + LiDFBP after 50cycles at 45 °C.



**Figure 36** shows the C 1s, F 1s, and O 1s XPS spectra for the gra-SiC anodes cycled with Carbonate, EME and EME + LiDFBP after 50 cycles at 45°C. In C 1s spectra, the anodes with EME appears a remarkable reduction of the peak intensity assigned to C-C, compared to the anode with Carbonate (**Figure 36a, d**). The decrease in the C-C peak intensity is due to the thick SEI layer formed by EME electrolyte during cycling test. During cycling, the SEI layer becomes thick due to decomposition of EME at high temperature and deposition of metal ions as shown in **Figure 37**. On the other hand, with EME + LiDFBP electrolyte, the peak intensity assigned to the C-C is the highest among three electrolytes as shown in **Figure 36g**. This finding corresponds to the cross-sectional SEM images of the anode cycled with EME + LiDFBP (**Figure 35f**). In F 1s spectra, by replacing Carbonate with EME, the relative fraction of LiF increased from 70.2% to 80.7% and the relative fraction of NiF<sub>2</sub> increased from 13.3% to 14.4% (**Figure 36b, e**). The result indicates that the SEI layer formed by EME electrolyte was not able to protect cathode from HF attack during cycling test. On the other hand, by using LiDFBP additive, the relative fraction of LiF decreased from 80.7% to 68.4% and the relative fraction of NiF<sub>2</sub> decreased from 14.4% to 13.6% (**Figure 36e, h**). LiDFBP successfully protects the anode from HF attack and prevented metal ions dissolution of the NCM cathode during cycling test. The formation of LiF and NiF<sub>2</sub> consumes active materials, thus the reduction of LiF and NiF<sub>2</sub> means mitigation of capacity fading. In the O 1s spectra, the peak of ROLi at 528.5 eV is noticeable. With EME electrolyte, the peak intensity of ROLi is the highest among three electrolytes (**Figure 36f**). The thick and non-uniform SEI layer derived by the EME electrolyte after cycle test consists of a large amount of ROLi. In addition, the increased ROLi peak also indicates the formation of dendritic Li, which is a good agreement with the SEM image of the cycled anode with EME (**Figure 35b**). With the LiDFBP containing electrolyte, the ROLi peak intensity decreases, compared to EME electrolyte. LiDFBP effectively suppresses the continuous decomposition of EME solvent during cycling test(**Figure 38**).

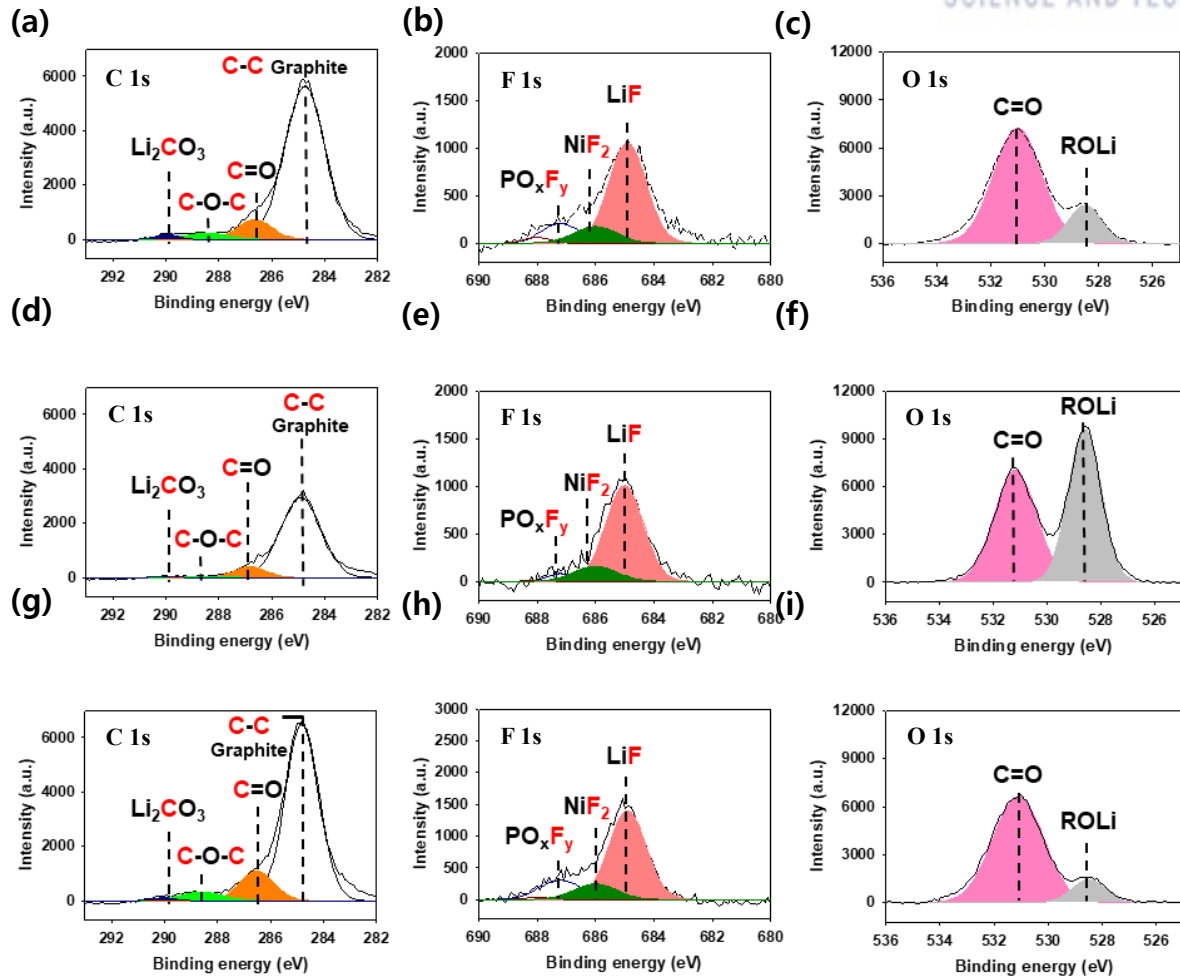


**Figure 36.** C 1s, F 1s, and O 1s XPS spectra of NCM811 cathodes from NCM811/gra-SiC full cells after 50 cycles at 45°C (Carbonate : (a), (b), (c); EME : (d), (e), (f); and EME + LiDFBP : (g), (h), (i)).

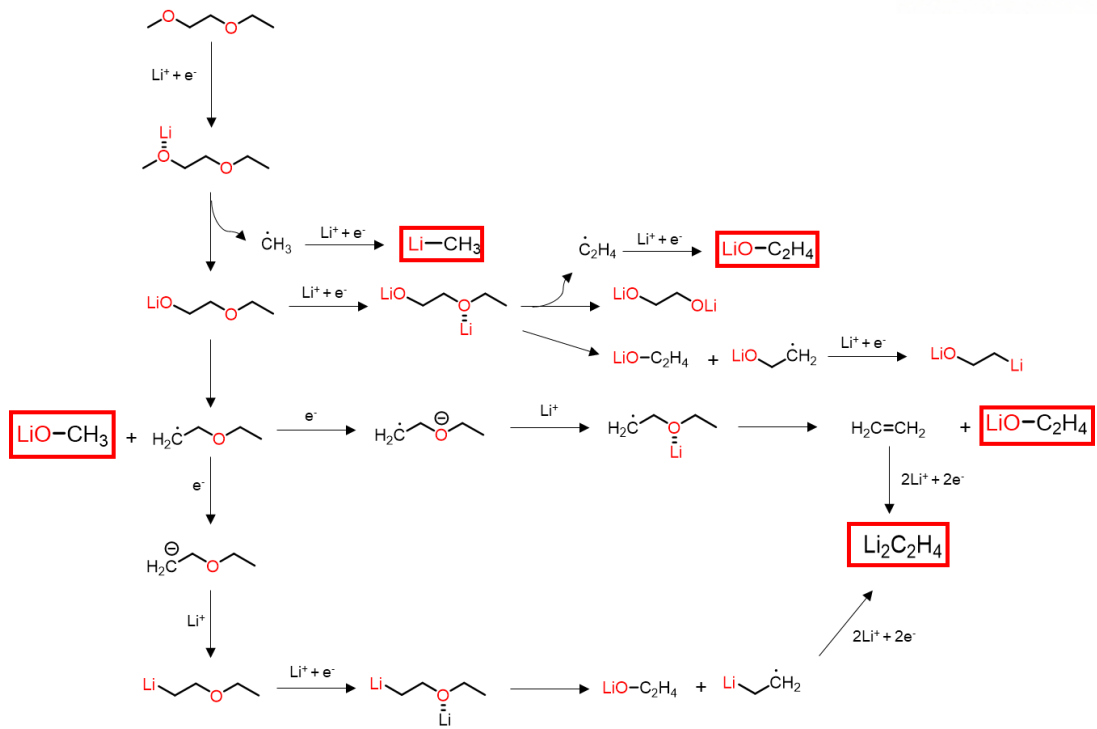


Figure 37. Possible decomposition mechanisms of EME.

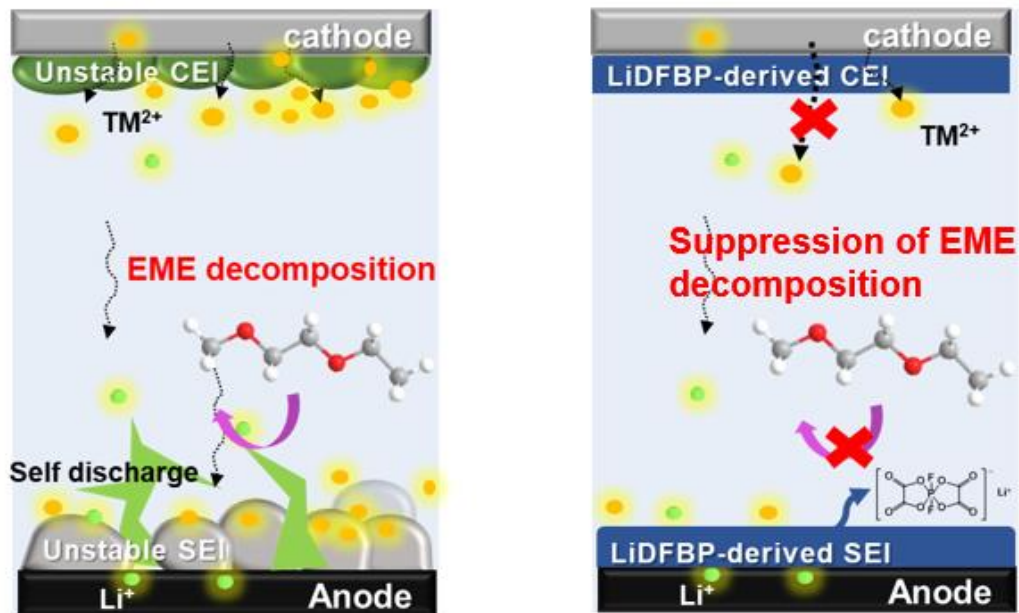


Figure 38. Schematic illustration of beneficial effects of LiDFBP on the anode.

### 3. Conclusion

In this study, the introduction of low-viscosity EME solvent and LiDFBP additive improves fast charging capability and cycling stability at high temperature. The EME electrolyte with low viscosity improves ionic conductivity and lowers cell impedance, enhancing the impregnation of electrolyte into the high-mass-loading-electrode. XRD data of the NCM811 cathode after charging at a rate of 4C reveals facile delithiation in the EME electrolyte. In terms of volatility, thanks to high boiling point of EME, less gas evolution is observed through TGA and pouch swelling test. However, dQ/dV plot, transition metal dissolution test and LSV revealed that CEI and SEI formed by EME solvent are unstable at high temperature.

To solve the problems caused by EME solvent, LiDFBP additive is introduced. The dQ/dV plot shows that LiDFBP decomposes before EME, forming stable SEI layer. Based on the XPS analysis, LiDFBP additive produces C=O based stable and thin surface film. The stable CEI layer prevented the generation of microcracks during cycling with 4C charge and 1C discharge at 45°C, mitigating transition metal dissolution from the cathode and capacity fading. Ni 2p spectra of the cycled anode reveals the reduction of NiF<sub>2</sub> deposition on the anode. SEM images after 50 cycles at 45°C display the effect of LiDFBP on electrolyte decomposition. The SEI layer with EME + LiDFBP after 50cycles was thin and uniform without dendritic Li. XPS spectra of gra-SiC anodes after cycle test indicates that unstable ROLi is the main component of SEI formed by EME decomposition.

Consequently, the introduction of LiDFBP additive to EME solvent modified both SEI and CEI layer enhancing the cycling performance at high temperature. Using EME and LiDFBP reported the synergistic effects which contributed to thermal stability and fast charging capability.

## REFERENCES

1. Kabir, M.M. and D.E. Demirocak, *Degradation mechanisms in Li-ion batteries: a state-of-the-art review*. International Journal of Energy Research, 2017. **41**(14): p. 1963-1986.
2. Lu, L., et al., *A review on the key issues for lithium-ion battery management in electric vehicles*. Journal of Power Sources, 2013. **226**: p. 272-288.
3. Thackeray, M.M., C. Wolverton, and E.D. Isaacs, *Electrical energy storage for transportation—approaching the limits of, and going beyond, lithium-ion batteries*. Energy & Environmental Science, 2012. **5**(7): p. 7854-7863.
4. Choi, N.-S., et al., *Challenges Facing Lithium Batteries and Electrical Double-Layer Capacitors*. Angewandte Chemie International Edition, 2012. **51**(40): p. 9994-10024.
5. Nitta, N., et al., *Li-ion battery materials: present and future*. Materials Today, 2015. **18**(5): p. 252-264.
6. Liu, W., et al., *Nickel-rich layered lithium transition-metal oxide for high-energy lithium-ion batteries*. Angew Chem Int Ed Engl, 2015. **54**(15): p. 4440-57.
7. Manthiram, A., *A reflection on lithium-ion battery cathode chemistry*. Nature Communications, 2020. **11**(1): p. 1550.
8. Bak, S.-M., et al., *Structural changes and thermal stability of charged LiNi<sub>x</sub>Mn<sub>y</sub>Co<sub>z</sub>O<sub>2</sub> cathode materials studied by combined in situ time-resolved XRD and mass spectroscopy*. ACS applied materials & interfaces, 2014. **6**(24): p. 22594-22601.
9. Ryu, H.-H., et al., *Capacity Fading of Ni-Rich Li[Ni<sub>x</sub>Co<sub>y</sub>Mn<sub>1-x-y</sub>]O<sub>2</sub> (0.6 ≤ x ≤ 0.95) Cathodes for High-Energy-Density Lithium-Ion Batteries: Bulk or Surface Degradation?* Chemistry of Materials, 2018. **30**(3): p. 1155-1163.
10. Lu, J., et al., *High-Performance Anode Materials for Rechargeable Lithium-Ion Batteries*. Electrochemical Energy Reviews, 2018. **1**(1): p. 35-53.
11. Liang, J., et al., *Facile synthesis of ceramic SiC-based nanocomposites and the superior electrochemical lithiation/delithiation performances*. Materials Chemistry and Physics, 2020. **243**: p. 122618.
12. Choi, J.W. and D. Aurbach, *Promise and reality of post-lithium-ion batteries with high energy densities*. Nature Reviews Materials, 2016. **1**(4): p. 16013.
13. Du, Z., et al., *Understanding limiting factors in thick electrode performance as applied to high energy density Li-ion batteries*. Journal of Applied Electrochemistry, 2017. **47**(3): p. 405-415.
14. Son, H.B., et al., *Effect of reductive cyclic carbonate additives and linear carbonate co-solvents on fast chargeability of LiNi<sub>0.6</sub>Co<sub>0.2</sub>Mn<sub>0.2</sub>O<sub>2</sub>/graphite cells*. Journal of Power Sources, 2018.

- 400**: p. 147-156.
15. Xu, K., *Electrolytes and interphases in Li-ion batteries and beyond*. Chem Rev, 2014. **114**(23): p. 11503-618.
  16. Logan, E.R., et al., *A Study of the Physical Properties of Li-Ion Battery Electrolytes Containing Esters*. Journal of The Electrochemical Society, 2018. **165**(2): p. A21-A30.
  17. Wang, J., et al., *Superconcentrated electrolytes for a high-voltage lithium-ion battery*. Nat Commun, 2016. **7**: p. 12032.
  18. Hall, D.S., et al., *Exploring Classes of Co-Solvents for Fast-Charging Lithium-Ion Cells*. Journal of The Electrochemical Society, 2018. **165**(10): p. A2365-A2373.
  19. Sasaki, Y., et al., *Physical and Electrolytic Properties of Partially Fluorinated Organic Solvents and Its Application to Secondary Lithium Batteries: Partially Fluorinated Dialkoxyethanes*, in *ECS Transactions*. 2009, **16**(35): p. 23-31.
  20. Kim, K., et al., *Electrolyte-Additive-Driven Interfacial Engineering for High-Capacity Electrodes in Lithium-Ion Batteries: Promise and Challenges*. ACS Energy Letters, 2020. **5**(5): p. 1537-1553.
  21. Kim, C.-K., et al., *Synergistic Effect of Partially Fluorinated Ether and Fluoroethylene Carbonate for High-Voltage Lithium-Ion Batteries with Rapid Chargeability and Dischargeability*. ACS Applied Materials & Interfaces, 2017. **9**(50): p. 44161-44172.
  22. Kim, K., et al., *Understanding the thermal instability of fluoroethylene carbonate in LiPF<sub>6</sub>-based electrolytes for lithium ion batteries*. Electrochimica Acta, 2017. **225**: p. 358-368.
  23. Michan, A.L., et al., *Fluoroethylene Carbonate and Vinylene Carbonate Reduction: Understanding Lithium-Ion Battery Electrolyte Additives and Solid Electrolyte Interphase Formation*. Chemistry of Materials, 2016. **28**(22): p. 8149-8159.
  24. Jung, R., et al., *Consumption of Fluoroethylene Carbonate (FEC) on Si-C Composite Electrodes for Li-Ion Batteries*. Journal of The Electrochemical Society, 2016. **163**(8): p. A1705-A1716.
  25. Jaumann, T., et al., *Lifetime vs. rate capability: Understanding the role of FEC and VC in high-energy Li-ion batteries with nano-silicon anodes*. Energy Storage Materials, 2017. **6**: p. 26-35.
  26. Han, J.G., et al., *Interfacial Architectures Derived by Lithium Difluoro(bisoxalato) Phosphate for Lithium-Rich Cathodes with Superior Cycling Stability and Rate Capability*. ChemElectroChem, 2017. **4**(1): p. 56-65.
  27. Kim, K.-E., et al., *A combination of lithium difluorophosphate and vinylene carbonate as reducible additives to improve cycling performance of graphite electrodes at high rates*. Electrochemistry Communications, 2015. **61**: p. 121-124.
  28. Niu, C., et al., *High-energy lithium metal pouch cells with limited anode swelling and long*

- stable cycles*. Nature Energy, 2019. **4**(7): p. 551-559.
29. Tian, J., et al., *Enhanced Performance of PbS-quantum-dot-sensitized Solar Cells via Optimizing Precursor Solution and Electrolytes*. Scientific Reports, 2016. **6**: p. 23094.
  30. Li, Y., et al., *Three-dimensional fusiform hierarchical micro/nano Li<sub>1.2</sub>Ni<sub>0.2</sub>Mn<sub>0.6</sub>O<sub>2</sub> with a preferred orientation (110) plane as a high energy cathode material for lithium-ion batteries*. Journal of Materials Chemistry A, 2016. **4**(16): p. 5942-5951.
  31. Qian, K., et al., *Abuse tolerance behavior of layered oxide-based Li-ion battery during overcharge and over-discharge*. RSC Advances, 2016. **6**(80): p. 76897-76904.
  32. De Biasi, L., et al., *Chemical, Structural, and Electronic Aspects of Formation and Degradation Behavior on Different Length Scales of Ni-Rich NCM and Li-Rich HE-NCM Cathode Materials in Li-Ion Batteries*. Advanced Materials, 2019. **31**(26): p. 1900985.
  33. Hawley, W.B., et al., *Lithium and transition metal dissolution due to aqueous processing in lithium-ion battery cathode active materials*. Journal of Power Sources, 2020. **466**: p. 228315.
  34. Han, J.-G., et al., *Scavenging Materials to Stabilize LiPF<sub>6</sub>-Containing Carbonate-Based Electrolytes for Li-Ion Batteries*. Advanced Materials, 2019. **31**(20): p. 1804822.
  35. Park, K.-J., et al., *Degradation Mechanism of Ni-Enriched NCA Cathode for Lithium Batteries: Are Microcracks Really Critical?* ACS Energy Letters, 2019. **4**(6): p. 1394-1400.
  36. Kim, K., et al., *Cyclic Aminosilane-Based Additive Ensuring Stable Electrode–Electrolyte Interfaces in Li-Ion Batteries*. Advanced Energy Materials, 2020. **10**(15): p. 2000012.
  37. Freiberg, A.T.S., et al., *Li<sub>2</sub>CO<sub>3</sub> decomposition in Li-ion batteries induced by the electrochemical oxidation of the electrolyte and of electrolyte impurities*. Electrochimica Acta, 2020. **346**: p. 136271.
  38. Jiao, S., et al., *Stable cycling of high-voltage lithium metal batteries in ether electrolytes*. Nat. Energy, 2018. **3**: p. 739-746.
  39. Mao, C., et al., *Identifying the limiting electrode in lithium ion batteries for extreme fast charging*. Electrochemistry Communications, 2018. **97**: p. 37-41.
  40. Foroozan, T., S. et al., *Mechanistic understanding of Li dendrites growth by in-situ/operando imaging techniques*. Journal of Power Sources, 2020. **461**: p. 228135.